Electro-Optics and Photonics Faculty Publications   Department of Electro-Optics and Photonics

4-2015

Tailoring Optical Complex Fields with Nano-Metallic Surfaces

Guanghao Rui
University of Dayton, grui01@udayton.edu

Qiwen Zhan
University of Dayton, qzhan1@udayton.edu

Review article

Guanghao Rui and Qiwen Zhan*

Tailoring optical complex fields with nano-metallic surfaces

Abstract: Recently there is an increasing interest in complex optical fields with spatially inhomogeneous state of polarizations and optical singularities. Novel effects and phenomena have been predicted and observed for light beams with these unconventional states. Nanostructured metallic thin film offers unique opportunities to generate, manipulate and detect these novel fields. Strong interactions between nano-metallic surfaces and complex optical fields enable the development of highly compact and versatile functional devices and systems. In this review, we first briefly summarize the recent developments in complex optical fields. Various nano-metallic surface designs that can produce and manipulate complex optical fields with tailored characteristics in the optical far field will be presented. Nano-metallic surfaces are also proven to be very effective for receiving and detection of complex optical fields in the near field. Advances made in this nascent field may enable the design of novel photonic devices and systems for a variety of applications such as quantum optical information processing and integrated photonic circuits.

*Corresponding author: Qiwen Zhan, Electro-Optics Program, University of Dayton, 300 College Park, Dayton, OH 45469, USA, e-mail: qzhan1@udayton.edu
Guanghao Rui: Advanced Photonics Center, Southeast University, Nanjing, Jiangsu, 210096, China; and Electro-Optics Program, University of Dayton, 300 College Park, Dayton, OH 45469, USA

Edited by Volker Sorger

1 Introduction

As electromagnetic wave governed by the Maxwell's equations, optical field is characterized by not only the scalar properties in terms of phase and amplitude, but also polarization arising from its vector nature. There has long been a pursuit for methods to comprehensively manipulate the behavior of light, namely the ability to control and modify the characteristics of light at will. In most cases, spatial variation of polarization within an optical field has been completely neglected and the study of wave optics can be reduced to a scalar wave equation, therefore the task of engineering of an optical field is reduced to spatially modulate the phase and/or amplitude. For example, in the field of adaptive optics, the ability to generate an arbitrary complex scalar optical field is useful and important in order to reconfigure the optical wavefront as quickly as possible. Owing to their versatility, spatial light modulators (SLMs) are the most popular choice for phase modulation of light that have been successfully demonstrated in many applications such as digital lenses, computer generated holograms, tunable filters and generation of optical fields with different orbital angular momentum (OAM) states, among many others.

In the last decade, there has been increasing number of cases in which the capability of creating arbitrary vectorial beam is desirable. Usually these so-called vectorial optical beams can be regarded as laser modes with additional spatial polarization modulations. The study of such vectorial optical fields has recently gained tremendous interests in a variety of applications ranging from super-resolution microscopy [1], laser micromachining [2], optical tweezers [3], to ellipsometry [4] and polarimetry [5]. These applications require the local control and manipulation over all parameters of the optical fields in terms of phase, amplitude and polarization. Significant amount of research has been conducted to develop versatile systems for the generation of the optical fields with exotic properties. Among many different types of devices, liquid crystal spatial light modulator (LC-SLM) is among the most popular due to its flexibility and capability. For examples,

arbitrary vector fields with inhomogeneous polarization distribution were reported using two transmissive SLMs [6], transmissive SLMs with Mach-Zehnder interferometry setup [7] and reflective phase-only LC-SLMs [8]. Another approach to generate and manipulate vectorial optical beams that has gained tremendous momentum recently is to use subwavelength structures, especially subwavelength metallic structures. Owing to the strong polarization dependence imposed by the boundary conditions at metal-dielectric interfaces, nano-metallic structures have been exploited to tailor the properties of the locally confined optical field as well as the scattered optical field in the far field [9]. In addition, for metals that can support plasmon polaritons, the plasmonic interactions enables efficient confinement and localization of optical fields, making them very attractive for applications such as photonic integrated devices and circuits.

More excitingly, theoretical and experimental developments in nanotechnology in the last decade have led to a bottom-up approach that enables researchers to design and manufacture artificial material with electronic, optical, thermal, mechanical and acoustic properties that may not be available naturally. For examples, photonic crystals are materials composed of periodic dielectric, metallo-dielectric or nanostructures that affect the propagation of optical wave in unexpected ways [10]. They are popular materials of study for applications in lasers, solar energy, light emitting diodes and more. Metamaterials are a novel class of artificial materials that allow to affect the properties of light by suitably chosen unit cells, called the meta-atoms [11]. The properties of this effective medium in turn are dictated by the chosen meta-atoms and their arrangement. Metamaterials are at the heart of many groundbreaking applications, such as a perfect lens that inhibits the refraction or a cloaking device that can hide objects from an external observer. However, a large body of research on photonics crystals and metamaterials has concentrated on three-dimensional (3D) structures that require complicated fabrication process. Recently the concept of flat optics in which the optical component is based on metasurfaces comprised of ultrathin metallic subwavelength structures was proposed and demonstrated with exotic properties when interacted with light [12]. This technique based on planar technology tremendously simplifies fabrication therefore is naturally better suited for large-scale applications.

When light pass through a photonic structure, the interaction between the photons and the structure strongly depends on the intrinsic properties of both the light and the constituting material. With the capability of spatially engineering both optical field and material properties on the subwavelength scale, much richer physics can be explored for various applications, such as optical inspection [13], super-resolving optical microscopy [1], display technologies [14], data storage [15], optical communications [16], and so on. In this paper, we review the recent progress and novel trend in the nascent technical area of optical complex fields and their interactions with nano-structured metallic thin film. Particularly we will focus on the nano-metallic structures that enable the generation or detection of various optical complex fields. In Section 2, we brief outline the concept of optical complex field, including the scalar vortex and polarization singularity, which are closely connected to the characteristics of the optical complex field. In Section 3, the introduction of plasmonic antenna and metasurface will be presented, including the key features of these metallic thin film structures such as polarization dependence, geometric phase effect, etc. In Section 4, we focus on the nano-metallic surface designs that enable the efficient generation and manipulation of optical complex fields in the far field. In Section 5, several nano-metallic surfaces designs that can be used to receive and detect various optical complex fields with high efficiency in the near field will be presented. In Section 6, a brief discussion on the applications of optical complex field and nano-metallic structure will be given.

2 Optical complex fields

Optical complex fields with unconventional spatial distributions in terms of polarization and phase are rapidly becoming a current trend due to the possibility of exploring the fundamental physics with numerous potential applications including information storage, processing and transportation [15], microscopic and nanoscopic imaging [17, 18], remote sensing [19, 20], materials micromachining and processing [2], etc. Among these optical complex fields, scalar vortex beam is one specific case that is characterized by a helical wavefront along with an optical singularity in the center [21, 22]. The optical vortex is a position in the beam cross section around which the optical phase advances or retards by a multiple of 2π. The phase at the vortex center is undefined, namely the term phase singularity. When projected onto a flat structure, a scalar vortex beam has a distribution of ring with a dark hole in the center. Therefore the vortex itself carries neither linear nor angular momentum (AM) due to the zero intensity. A scalar vortex beam in general is characterized by its topological charge l (l is integer), according to the number of twists that the light does in one wavelength.

The higher the number of the twist is, the faster the light is spinning around the axis. As a well-known class of optical scalar vortex beam, Laguerre-Gauss mode LG_{pl} has azimuthal symmetric intensity pattern and a helical phase structure described by $e^{il\phi}$, for which each photon carries OAM of $l\hbar$. Figure 1 shows the helical phase patterns and corresponding intensity distributions at the beam waist for Laguerre-Gauss modes with different topological charges. A dark center is shown in the intensity profiles with the phase pattern jumping from 0 to $l\cdot2\pi$ around the singularity point in the center. Besides, the size of the dark hole increases with the topological charge. Scalar vortex beams in various forms have been developed by a number of groups for different applications ranging from optical spanners in optical tweezers, and faster data manipulation in quantum computing, to twisted light for telecommunications [21].

Besides the scalar vortex, vectorial optical field with polarization singularities is another example of the optical complex field that has been intensively studied. These type of beams have spatially variant state of polarization (SOPs) depending on the spatial location in the beam cross section. This is distinctively different with the optical beams dealt by most past research that have spatially homogeneous SOPs, such as linearly, circularly and elliptically polarized beams. With carefully arranged spatial SOP distributions, optical systems with extended functionalities and capabilities can be envisioned. Cylindrical vector (CV) beam is the most well-known example with the cylindrical symmetry in polarization and polarization singularity in the center of the beam cross section [23]. Radial and azimuthal polarizations are the two specific examples of CV beam which have the electric field aligned along radial and azimuthal directions, respectively. Due to the orthogonality, these two modes form complete set of bases for CV beam. Consequently, any generalized CV beam can be represented by the combination of radial and azimuthal modes with different weights (Figure 2). In the past decade, the axisymmetric polarization distribution and unique focusing properties of CV beams under high numerical aperture (NA) condition were exploited by researchers with potential applications in imaging, machining, particle trapping, data storage, and sensing [23], etc.

3 Plasmonic antennas and metasurfaces

Nowadays, controlling and guiding light has been one of the most influential scientific achievements. It affects
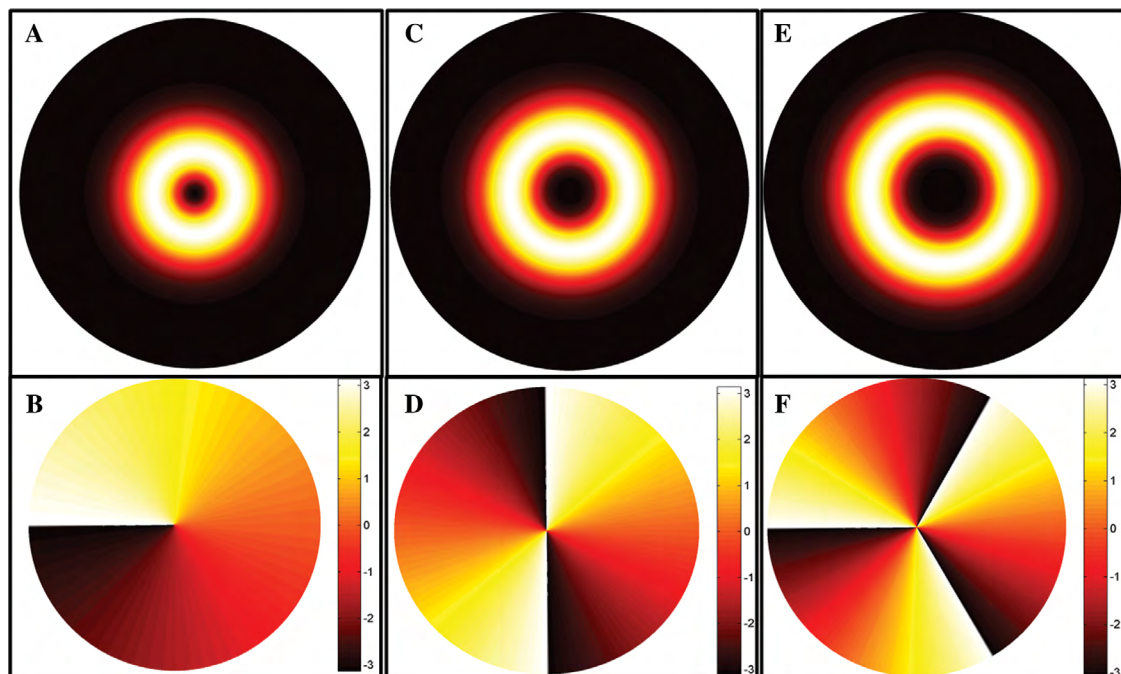

Figure 1 Intensity distributions (A, C, E) and corresponding helical phase patterns (B, D, F) at the focal plane for LG_{01}, LG_{02} and LG_{03} modes of vortex beams. The LG_{lp} modes are associated with phase patterns described as $e^{il\phi}$, with ϕ being the azimuthal angle and l being the azimuthal index.
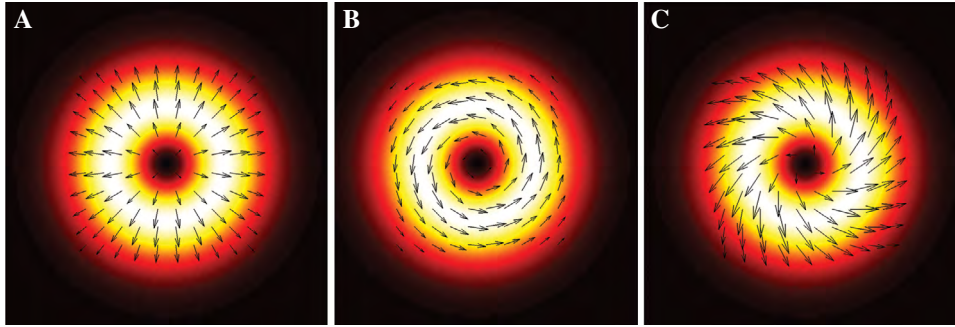
Figure 2   CV beams: (A) radially polarized beam $r \times e^{-r^2/w^2}\vec{e}_r$; (B) azimuthally polarized beam $r \times e^{-r^2/w^2}\vec{e}_\phi$; (C) generalized CV beam, which is a linear superposition of (A) and (B).

daily life in many ways, such as the development of telescope, microscopes, spectrometers, and optical fibers, etc. These examples utilize the wave nature of light and are based on the modification of the wavefront of light by optical elements such as mirrors, lens, and prisms. Due to the inevitable diffraction effect arising from the dielectric optics, optical fields cannot be localized within dimensions much smaller than the optical wavelength, which limits the resolution to which an object can be imaged, as well as the size of the transverse cross section of efficient guiding structures to the wavelength dimension.

When light interacts with a metallic nanostructure, the free electrons inside the metal can be driven by the incident photons in collective oscillations known as surface plasmon polaritons (SPPs) [24]. During the last decade, SPPs has attracted lots of research interests due to its intriguing properties such as high local field enhancement and short effective wavelength. SPPs can be focused into a tightly confined spot with the size beyond the diffraction limit with a highly focused laser beam excitation, or a plasmonic antenna. Plasmonic antennas, also known as optical antennas, are nanometer-sized metallic structures that scale down the concept of conventional radio frequency antennas and resonate at optical frequencies [25]. Plasmonic antennas allow one to mediate radiation from an external source to a nanoscopic region or assist a nanometric light source to emit efficiently into the far field, depending on whether it is operated as a receiver or emitter. The research in the field of plasmonic antenna is currently driven by the need for high field enhancement, strong field localization, and large absorption cross sections, which finds the applications in high-resolution microscopy, spectroscopy, photovoltaic, light emission, and coherence control.

Since metals can no longer be considered as perfect conductors in the visible spectrum regime, the plasmonic character of optical antennas needs to be fully respected. The properties of the plasmonic antennas may be strongly shape and material dependent owing to surface plasmon resonances (SPRs). For a subwavelength metallic geometry, usually more than one type of SPR exists corresponding to different wavelengths and polarizations of the excitation. Consequently, similar to their radiofrequency counterparts, plasmonic antennas are intrinsically polarization sensitive elements. For example, slot antenna was explored to be served as localized polarizer because only the electric field oscillating along the direction perpendicular to the aperture would excite localized waveguide mode in the rectangular aperture, leading to an enhanced transmission also known as extraordinary optical transmission effect [26].

In an anisotropic and inhomogeneous medium, otherwise independent spin angular momentum (SAM) and OAM can be made to interact, changing both the polarization and phase of the optical field [27]. This change depends on the polarization of the incident light and the topology of the medium, the relationship of which can be described by the concept of geometric phase (or Pancharatnam–Berry phase) [28]. Recently, this phenomenon has enabled geometric phase devices that control the wavefront of the output beam according to the polarization of the illumination. It can be created by coupled isotropic scatters [29], or using anisotropic subwavelength scatters with spatially varying orientations [30, 31]. Bull's eye plasmonic antenna is another type of structure that enables the spin-orbit interaction. Considering a bull's eye structure that consists of a single annular slot, it can be regarded as a series of subwavelength slot antennas with identical geometric parameters but spatially oriented with radial symmetry. When the bull's eye structure is normally illuminated by a circularly polarized light, the transmitted field of every single slot aperture with orientation angle of α is linearly polarized along α-direction and carries an additional geometric phase of α. Therefore the entire structure with α ranging from 0 to 2π will imprint a spiral phase distribution to the transmitted wavefront,

creating a vortex beam with topological charge $|l|=1$ [32]. Consequently, the geometric phase results from the spin-orbit angular momentum coupling due to the space-variant polarization state and directional manipulations and is therefore geometric in nature.

In dielectric optics using bulk materials, tailoring of optical field in terms of phase, amplitude and polarization is achieved by sculpting the optical wavefront as the optical wave propagating through the dielectric optical element. The changes of properties of the optical fields are accumulated through the propagating along specific optical path that can be controlled by engineering the dielectric of the optical element. However, due to the reliance on the propagating effect, the entire system is hard to be integrated because increasing number of elements is required and leading to cumbersome light modulation process. Recently, a novel concept of "metasurface" was proposed to comprehensively engineer the optical field with only one flat surface [9, 12, 33]. Usually metasurface is made of arrays of plasmonic antennas with sub-wavelength separation. Different from dielectric optics, the essence of metasurface is to form a spatially varying optical response by using plasmonic antennas with spatially varying geometries, and the shaping of wavefront is realized by introducing an abrupt phase changes over the scale of the wavelength. The dispersion and anisotropic properties of plasmonic antennas give rise to the feasibility of tailoring amplitude, phase, as well as polarization response of the scattering field. For example, the SPR of a nanorod antenna SPR occurs when the length of the nanorod equals to one half of the SPPs wavelength. Under monochromatic excitation, the current excited in the nanorod would lag or lead the driving field by adjusting the length of the nanorod, depending on the length is longer or shorter than its resonant length, giving rise to a scattering field with controllable phase modulation. Using this concept, a metasurface capable of introducing a constant gradient of phase jump along the interface was designed. Figure 3A shows the scanning electron microscope (SEM) images of the fabricated metasurface in which the unit cell of the metasurface comprises eight V-shaped antennas with different geometrical parameters and orientations. The advantage of V-shaped antenna over the rod structure is the large tuning range of the phase which could cover the entire 2π range owing to multiple independent resonances [9]. Each single scatter in one unit cell is designed to obtain equal amplitude and constant phase difference of the cross-polarized scattering field. The entire metasurface with these symmetry-breaking plasmonic antennas imprint a linear distribution of the phase shift (from 0 to 2π) to the wavefront, giving rise to anomalous reflection and refraction phenomena (shown in Figure 3B). Furthermore, the concept of optical phase discontinuities provides possible pathway for building aberration-free planar lenses and axicons. Flat lenses both at telecom and visible wavelength have been experimentally demonstrated using V-shaped antennas [34, 35]. Along with different shapes of the antenna elements, the NA of the lens can be arranged in concentric rings that the abrupt phase shifts cause the wave propagating through the interface to experience a fully constructive interference at the focus.

Compared with the bulk metamaterials, nano-metallic surfaces exhibit unique advantages in controlling light
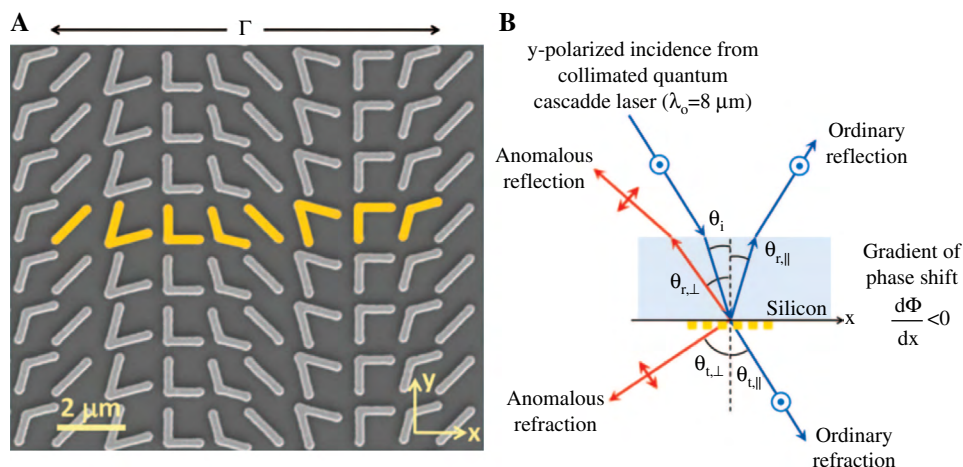

Figure 3 (A) SEM image of a plasmonic antenna array fabricated on a silicon wafer. The unit cell of the metasurface comprises eight gold V-shaped antenna with a periodicity $\Gamma=11\,\mu m$ in the x direction. (B) A gradient of interfacial phase jump $d\phi/dx$ provides an effective wavevector along the interface that can bend cross-polarized transmitted and reflected light into arbitrary directions. Adapted from Ref. [9].

propagation with extraordinary abilities. The ultrathin nano-metallic surfaces can be easily integrated with other on-chip optical devices, which is highly desirable for miniaturized photonic system. Both the loss and cost arising from Ohmic loss of metal and fabrication can also be reduced owing to the reduced size and volume. Finally, the development of nano-metallic surfaces benefit from diverse plasmonic antenna designs, allowing one to adopt a wide variety of antenna designs from the existing microwave and radio frequency antenna theory to meet specific requirements. Combining the added degrees of freedom offered by the optical complex field and the flexibility of nano-metallic surfaces, new types of devices that allow efficient engineering/interaction with optical complex fields can be envisioned.

4 Generation and manipulation of optical complex fields with nano-metallic surfaces in the far field

4.1 Generation of radial polarization

Radially polarized beam is one of the mostly intensively studied vectorial optical field. It has been shown that radially polarized beam is the optimal SPP excitation source for plasmonic structure with axial symmetry [36, 37]. The tiny focal spot (beyond the diffraction limit) produced by such a combination of radial polarization symmetry and the axial symmetry of the plasmonic structure make it attractive for a variety of applications [23]. The availability of a compact and highly efficient radially

polarized source is desirable for the further development of these applications to be practical. Various active or passive methods are proposed to generate the radially polarized beam, such as inserting specially designed elements into a laser resonator, or using few-mode fiber [23]. However, most setups are bulky and require precise alignment. A compact and flexible all-fiber design for radially polarized beam generation is reported by fabricating subwavelength concentric metallic grating on the facet of an optical fiber [38]. Figure 4 shows the SEM images of the fiber based concentric grating and a zoom-in of the metallic annular structure. When an azimuthal polarized beam is focused onto the bull's eye structure, the entire beam is TE polarized with respect to the axially symmetric metallic grating and therefore experiences a high reflection. In contrary, a radially polarized beam is entirely TM polarized with respect to the metallic grating and can pass through the device with higher transmittance than the azimuthal polarization. If a circularly polarized beam is focused into a fiber with concentric ring integrated on the core region, the output beam from the end of the fiber is radially polarized because the circular polarization can be decomposed into a linear superposition of uniformly distributed radial and azimuthal polarization components. Figure 5A shows the total intensity distribution of the output laser beam captured by a CCD camera. The dark spot in the center reveal the polarization singularity obtained by the CV beam and the polarization of the output beam is analyzed by a linear polarizer oriented at different angles (shown in Figure 5B). Note that the beam can be conveniently converted into an azimuthally polarized beam with two cascaded half-wave plates. This approach eliminates the needs of conventional conical devices or birefringent crystals in fiber laser cavity,
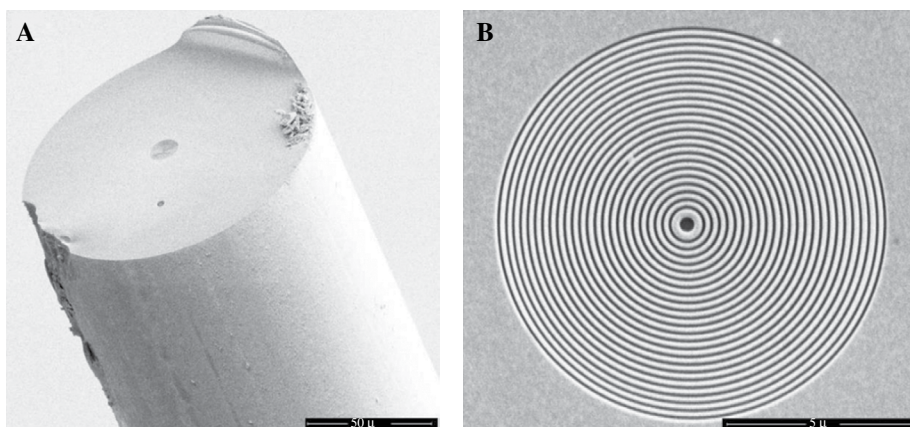

Figure 4 SEM image of (A) 20 periods of concentric metallic rings fabricated onto fiber end and (B) zoom-in of the metallic grating. Adapted from Ref. [30].
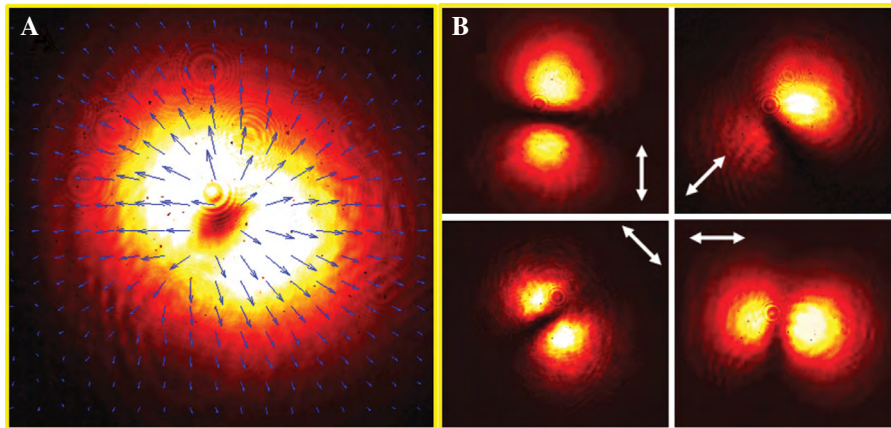
Figure 5 (A) CV beam generated at the fiber end with circularly polarized illumination. (B) CV beam passes through a linear analyzer oriented at different angles indicated by the arrows. Adapted from Ref. Adapted from Ref. [30].

providing a compact and convenient way for CV beam generation with fiber laser.

In free space, a convenient way to generate pure radial polarization is to let a circularly polarized light passing through a radial polarizer followed by a spiral phase plate [23]. Recently, the roles of these two elements were replaced by a novel nanostructured hologram that capable of manipulating both amplitude and phase information of light over a broad spectrum [39]. As shown in Figure 6A, the large opening of the hologram is filled with subwavelength apertures arrays, which is oriented to locally select a particular polarization state. The complex hologram is designed to create a radially polarized beam from an incident circularly polarized Gaussian beam. The wire-grid polarizer is used to filter out the azimuthal polarization and the functionality of the binary fork hologram is to impose a conjugate spiral phase so as to compensate the geometric phase arising from the projection of circular polarization to the cylindrical coordinates. Figure 6C shows the far-field intensity with the excitation wavelength
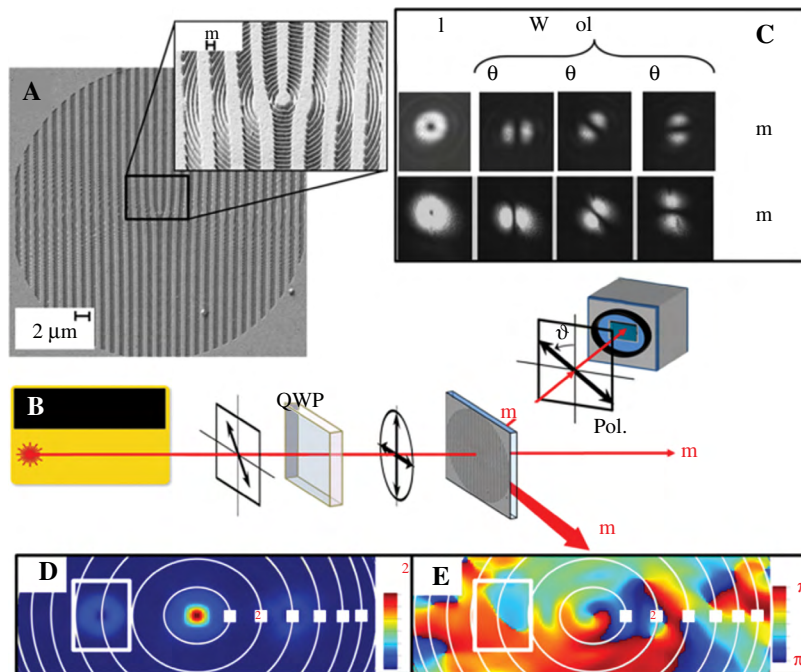

Figure 6 (A) SEM image of the fabricated hologram. (B) Experimental setup. (C) Measured far-field intensity distributions at two wavelengths, with and without the linear polarizer. The transmission axis of the polarizer is indicated by the arrows. Simulated far-field (D) intensity and (E) phase profiles plotted in polar coordinates. Adapted from Ref. [31].

of 633 nm and 850 nm captured by a CCD camera located at the m=+1 diffraction order of the hologram (Figure 6B). The purity of the generated radial polarization is checked by inserting an analyzer before the CCD camera with different orientation angles. At both wavelengths, the output beams exhibit similar quality and characteristics. It is worthy of noting that the OAM imposed by the hologram changes with the diffraction order. For diffraction order of m, the phase modulation can be expressed as $e^{jm\theta}$. Figure 6D, E show the simulated far-field intensity and phase profiles including three diffraction orders (m=0, ±1). It can be seen that only the beam at the m=+1 order has flat phase front distribution, giving rise to a pure radial polarization. A twin image with conjugate phase modulation shows up in the m=-1 order. The beam propagating along this direction carries a phase factor of $e^{2j\theta}$ due to the additional angular momentum acquired in scattering off the holographic grating. At the 0th diffraction order, the beam is solid and still radially polarized, however presents a nonvanishing topological charge of 1. The transmission efficiency of this metallic hologram depends on the desired polarization state of the transmitted light. In this case, the conversion efficiency of the radially polarized beam is calculated to be about 3.95%. The ability to appropriately shape amplitude, phase, and polarization of light over a broadband with a single ultrathin hologram allows the generation of high-order Bessel and Airy beam generation and this technology may find widespread applications in the fields of photonics.

4.2 Beaming photons with spin and orbital angular momentum

Recent rapid advances in plasmonic antenna offer tremendous opportunities to implement comprehensive control of the emission characteristics from nanoscale quantum emitters, which would be extremely attractive for many applications ranging from single molecular sensing to spin

optics and quantum information processing. In radiofrequency antenna engineering, it is well known that right hand or left hand circular polarization (RHC and LHC) can be transmitted with spiral antenna with different handedness [40]. It has been demonstrated that it is feasible to construct a nanoscale circularly polarized photon source with unidirectional emission through coupling an electric dipole emitter to a spiral plasmonic antenna [41, 42]. The polarization of the emitted photon arises from the structural handedness of the spiral antenna that converts the electric dipole emission into far field. Highly directional far-field emission pattern can be realized through the use of the spiral antenna to improve its directivity. Let us consider right hand single Archimedes' spiral (RHS) with the coordinates for calculation shown in Figure 7. In the cylindrical coordinates, the RHS can be described as:

$$r = r_0 + \frac{m\lambda_{SPP}}{2\pi}\theta, \qquad (1)$$

where r_0 is a constant and λ_{SPP} is the SPPs wavelength on the metal/air interface, θ is the azimuthal angle and m can take arbitrary integer value. An electric dipole is located in the geometrical center with the oscillating direction normal to the spiral surface. The evanescent field emitted from the electric dipole would excite SPPs propagating along the spiral surface towards the spiral slot. The spiral edge can be thought of as an array of secondary SPPs point sources spatially ranged into a spiral pattern that reradiate into the free space on the other side of the dipole source. To understand the characteristic of this coupled emission, an analytical model has been built and it can be shown that with spiral pitch $\Lambda = \lambda_{SPP}$ (m=1), the optical far field can be described in the cylindrical coordinates as [43]:

$$E_x(z,\rho,\phi) = \vec{e}_x \pi r_0 \frac{\exp\left[ik_0\left(z+\frac{\rho^2}{2z}\right)\right]}{i\lambda_0 z}$$
$$\times E_0 \Delta r e^{\frac{i2\pi r_0}{\lambda_{SPP}}}\left[-J_2\left(-\frac{2\pi r_0 \rho}{\lambda_0 z}\right)e^{i2\phi} + J_0\left(-\frac{2\pi r_0 \rho}{\lambda_0 z}\right)\right], \qquad (2)$$
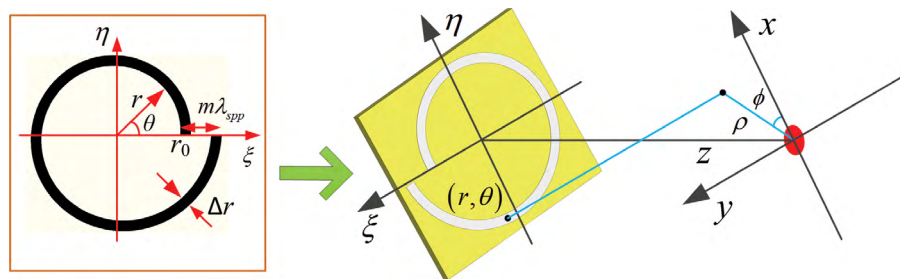

Figure 7 Illustration of a right hand spiral structure and the coordinates setup for the far field calculation. The inset illustrates the spiral structure viewed from the left and the coordinates used in the analytical calculation. Adapted from Ref. [35].

$$E_y(z,\rho,\phi) = -\vec{e}_y i\pi r_0 \frac{\exp\left[ik_0\left(z+\dfrac{\rho^2}{2z}\right)\right]}{i\lambda_0 z}$$
$$\times E_0 \Delta r e^{i\frac{2\pi r_0}{\lambda_{SPP}}}\left[-J_2\left(-\frac{2\pi r_0 \rho}{\lambda_0 z}\right)e^{i2\phi}\cdot J_0\left(-\frac{2\pi r_0 \rho}{\lambda_0 z}\right)\right]. \quad (3)$$

It can be seen that both x and y components have two terms and the total field is a superposition of two different modes proportional to the 0th and 2nd order Bessel functions. Due to the different transverse profiles of Bessel functions with lower and higher orders, the main lobe of the far-field distribution is given by the 0th order Bessel function and mostly attributed to the mode obtained RHC polarization. Figure 8 shows the experimental setup to validate the beaming effect of the spiral plasmonic antenna. Diluted quantum dots solution is adopted as the emitters dripped on the spiral surface. Note that it is critical to provide the correct feed to the spiral antenna. If the electric dipole oscillates in the plane parallel to the spiral surface, the far-field emission will spilt into two parts in the center and the emission polarization will be linear. Such a specific feed can be realized optically with the use of radially polarized excitation source due to its strong longitudinal component after highly focusing. The fluorescence emission on the other side of the sample is collected by an inverted high numerical aperture objective. Clearly, the directivity of the emission can be highly improved by the spiral antenna, which is manifested by the bright spot centered on the optical axis (Figure 9A–F).

The line-scans through the center of the emission patterns along x- and y-axes are shown in Figure 9G, H. It can be seen that higher fluorescence intensity and narrower angular width of the emission patterns can be obtained for spiral antenna with more turns. Besides, the emission in the far field is highly centered along the normal direction. For a spiral antenna with five turns, the emission pattern is highly directional, with FWHM of 10° and 11° along the x and y axes, respectively. The fluorescence peak intensity is increased up to 70-fold and the directivity is calculated to be 11.4 dB. The polarization property of the radiated emission is analyzed by a circular polarization analyzer composed of cascaded quarter-wave plate and linear polarizer. As shown in Figure 10, the field distribution after the LHC polarizer was totally disrupted while a central peak could also be observed when the emitted beam passes through a RHC analyzer, which is a manifestation of RHC polarization for the fluorescence emission. Circular polarization excitation ratio, which is defined as the ratio between the fluorescence intensities after LHC and RHC analyzer, respectively, is peaked near 10 in the center of the emission pattern. By changing the chirality of the spiral antenna, the handedness of the spin carried by the emitted photons will be reverted accordingly.

Besides beaming photons with specific polarization states at prescribed direction, the dipole-coupled spiral antenna has also been demonstrated for its capacity of dynamically steering the emission direction of photons by introducing a displacement of the feed point to the antenna [44]. Once the emitter is displaced from the
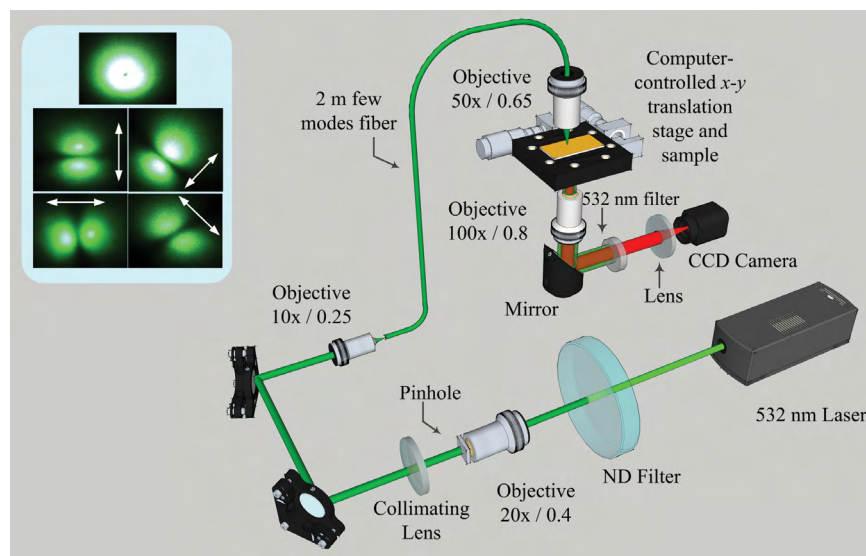

Figure 8 Experimental configuration. Inset shows the radially polarized beam generated at the end of the fiber, and the pictures of the beam after it passes through a linear polarizer orientated at different angles shown by the white arrows. Adapted from Ref. [34].
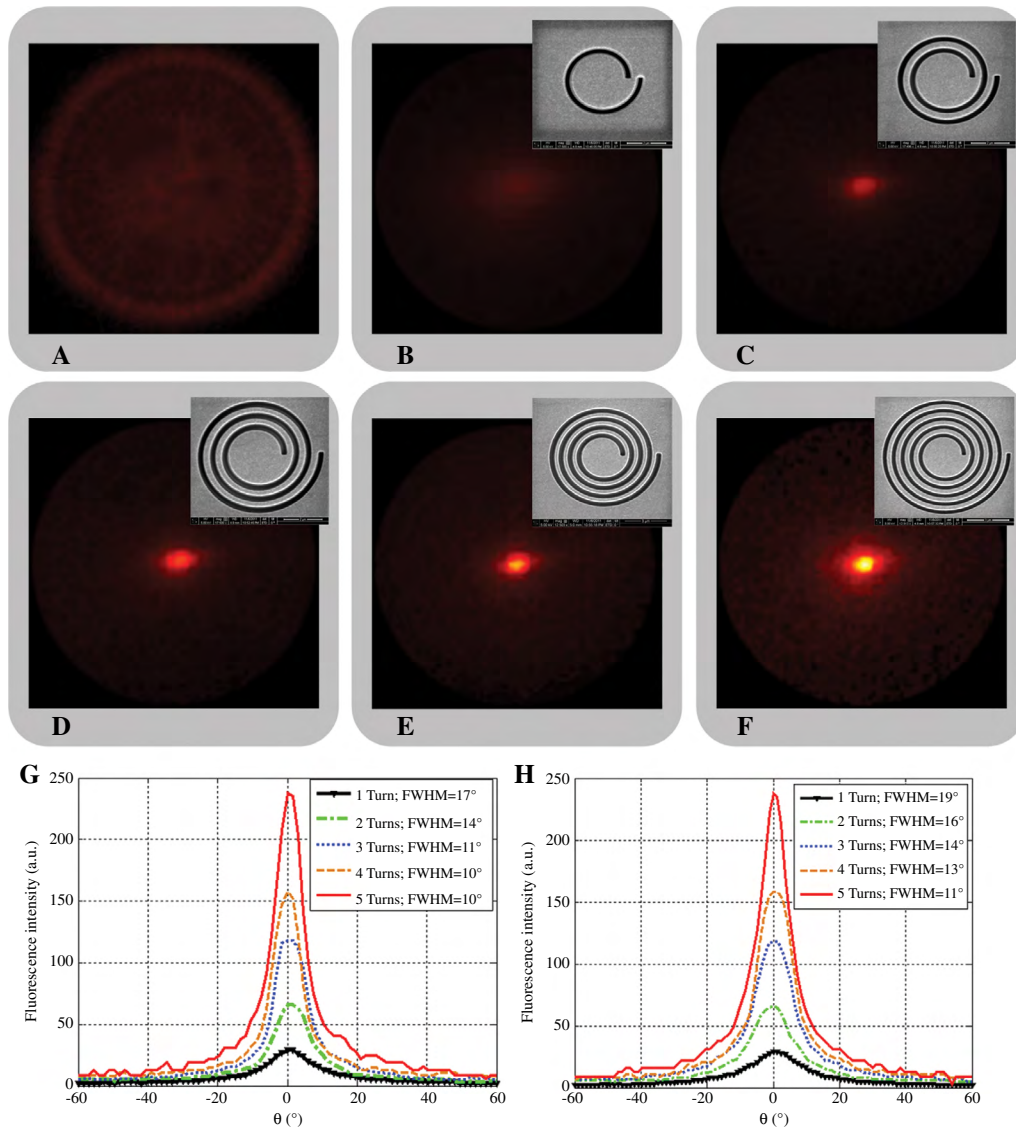
Figure 9 Fluorescence intensity distributions in the back focal plane of a 0.8 NA objective lens for (A) cover slip, and (B)–(F) right handed-ness spiral structure with an increasing number of turns from 1 to 5. SEM images of the spiral antennas are shown in the insets. Line-scans through the center of the emission pattern in the (G) x-z plane and (H) y-z plane. Adapted from Ref. [34].

geometrical center of the spiral antenna, the optical path difference from the edges of the device is no longer zero, leading to a tilt of the overall wavefront and the emission peak will shift from the normal direction accordingly. This beam steering mechanism can be explained by the interference of the transmitted waves from the spiral antenna. The optical path difference (OPD) Δl from the diametrically opposing sides of the antenna is calculated to be $\Delta l = 2\Delta r \times \lambda_0 / \lambda_{SPP}$, where Δr is the displacement of the dipole from the geometrical center of the antenna, λ_{SPP} and λ_0 are the wavelengths of the SPPs on the antenna surface and optical emission in the free space, respectively. When the dipole is displaced from the center, an overall wavefront

tilt is developed due to the non-zero OPD, leading to a shift of the far-field radiation peak from the normal direction with a steering angle θ:

$$\theta = \sin^{-1}(\Delta l / D), \qquad (4)$$

where D is the aperture size of the antenna. This simple equation enables us to estimate the steering angle of the far field emission, which increases linearly with larger displacement. The predicted beam steering phenomenon has been confirmed in the experiment. To realize the displacement of the feed point, the spiral sample is placed on a motorized translation stage. By moving the sample to specific location while keeping the excitation beam fixed,
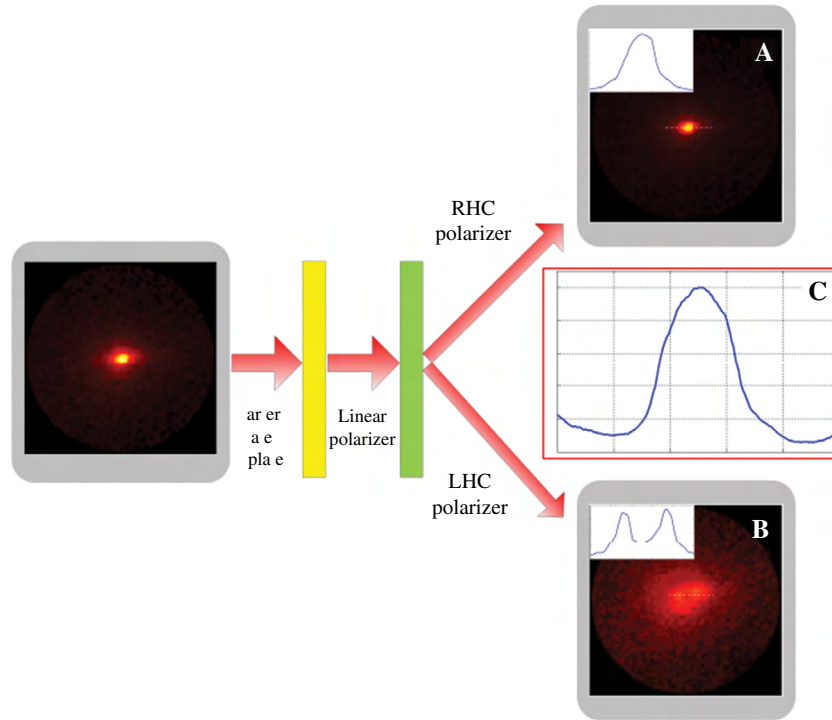
Figure 10 Methods for measuring the circular polarization extinction ratio of the fluorescence emission. The radiation emissions filtered by (A) a RHC polarizer and (B) LHC polarizer. (C) Line-scan of the circular polarization extinction ratio. Adapted from Ref. [34].

quantum dots in different areas within the spiral antenna are excited. When the excitation spot is away from the geometrical center of the spiral, the emission peak would shift from the normal direction accordingly. For the displacement of 200 nm and 500 nm, the steering angles are measured to be 3° and 7°, respectively (shown in Figure 11). In addition, the deflected far-field emission remains nearly the same angular width and polarization. Circular polarization extinction ratio of 8 and 7 are achieved for the displacements of 200 nm and 500 nm. Through continuous moving the translation stage in a prescribed way, dynamic steering of the photon emission has been realized as well.

More interestingly, if the pitch of the spiral is chosen to be other integer number multiplied with the SPPs wavelength, the photons emitted from the coupled structure will not only carry SAM but also OAM [43]. For $\Lambda = m \cdot \lambda_{\text{SPP}}$ ($m>1$), the optical far-field electric distribution can be found as [43]:

$$
E_x(z,\rho,\phi) = \vec{e}_x \pi r_0 \frac{\exp\left[ik_0\left(z+\frac{\rho^2}{2z}\right)\right]}{i\lambda_0 z} E_0 \Delta r e^{i\frac{2\pi r_0}{\lambda_{\text{SPP}}}}
$$
$$
\times \left[i^{m+1} J_{m+1}\left(-\frac{2\pi r_0 \rho}{\lambda_0 z}\right) e^{i(m+1)\phi} + i^{m-1} J_{m-1}\left(-\frac{2\pi r_0 \rho}{\lambda_0 z}\right) e^{i(m-1)\phi} \right].
$$

$$(5)$$

$$
E_y(z,\rho,\phi) = -\vec{e}_y i \pi r_0 \frac{\exp\left[ik_0\left(z+\frac{\rho^2}{2z}\right)\right]}{i\lambda_0 z} E_0 \Delta r e^{i\frac{2\pi r_0}{\lambda_{\text{SPP}}}}
$$
$$
\times \left[i^{m+1} J_{m+1}\left(-\frac{2\pi r_0 \rho}{\lambda_0 z}\right) e^{i(m+1)\phi} - i^{m-1} J_{m-1}\left(-\frac{2\pi r_0 \rho}{\lambda_0 z}\right) e^{i(m-1)\phi} \right].
$$

$$(6)$$

Similar to Eqs. (2) and (3), both the x and y components have two terms and the total electric field is a superposition of two different modes described by the $(m\text{-}1)^{\text{th}}$ and $(m\text{+}1)^{\text{th}}$ order Bessel functions. The exception is for the case of $m=0$ when the structure is reduced to a ring. For a spiral structure with $m>0$, it is interesting to notice that both of the two modes possess SAM and OAM simultaneously, but with reversed spin and different topological charges. The main lobe of the emission is mostly attributed to the mode obtained RHC polarization and OAM of $m\text{-}1$. The SAM and OAM carried by the emitted light are determined by the chirality and pitch of the spiral, respectively. This spin and pitch dependent focusing phenomena can be explained from the conservation of AM in a closed physical system. In this plasmonic system, the charity of the spiral structure is converted into SAM of the emitted photons, while the extra topological charge would be converted into OAM.
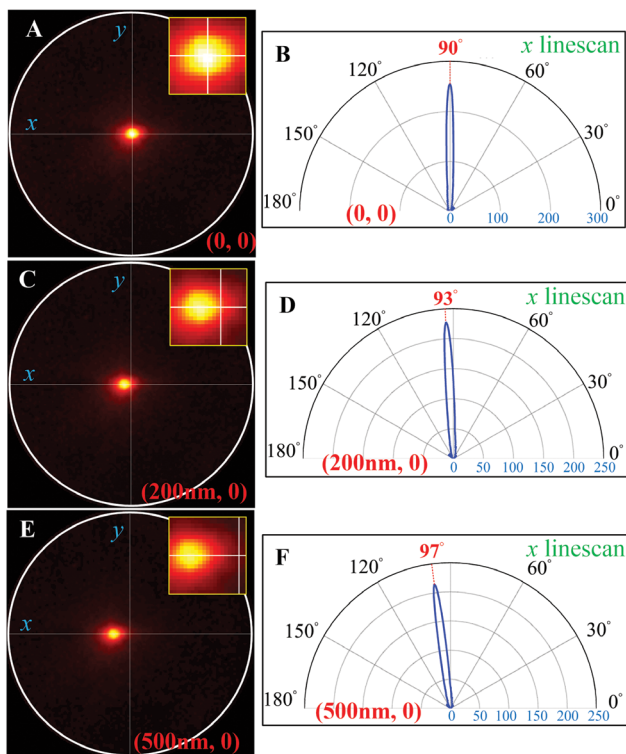
Figure 11 Fluorescence intensity distributions for different displacements of the feed point. For zero displacement: (A) intensity distribution, (B) line-scan in the x-z plane. For a displacement of 200 nm and 500 nm along the x axis: (C, E) intensity distribution, (D, F) line-scans in the x-z plane. Adapted from Ref. [36].

The AM selection rule existing in the spiral antenna system has been demonstrated by 3D finite element method model (COMSOL Multiphysics). Figure 12 shows the simulated far-field emission patterns for spiral antenna with different pitches. Besides the intensity distributions, the polarization maps of selected points superimposed on a zoom-in intensity distribution and zoom-in phase map are also shown. Good agreements have been obtained between the numerical simulation and analytical prediction in terms of the AM conversion for the main lobe. Consequently, as far as the main lobe is concerned, spiral plasmonic antenna with specifically designed pitch can be used to generate photons with both SAM and OAM states.

4.3 Generation of OAM-carrying vector beam with metasurface

At this point, we have introduced the nano-metallic surface being designed to generate and manipulate vector beam with polarization and phase singularities

separately. Recently a compact metasurface design was proposed to generate OAM carrying vectorial beam [45], which combines both twisted and vector features of the two typical categories of the vortex beam. As shown in Figure 13, the metasurface is consisted of slot antennas spatially arranged along a circle with gradually varied orientations, which enable to control both spatial phase and polarization simultaneously in the local spatial domain. Due to the strong polarization dependence of the slot antenna, each element can be regarded as a localized linear polarizer with the transmission axis perpendicular to the aperture direction. With such a spatially variant polarizer, a normally incident circularly polarized light can be converted into a vector beam with an order of l, where l denotes the number of rotation period of the slot antenna in one circle. In addition, this vector beam carry OAM with topological charge of $m=l\sigma$ attributed to the geometric phase, where σ denotes the SAM of the illumination. Figure 14 shows spatial distributions of phase and polarization of the output beams from six different configurations with l varies from +3 to -3 under excitation of LHC polarized light. The top row of the Figure 14 shows the spatial phase distribution of the field component perpendicular to the aperture direction. Cleary the OAM carried by the output beam varies from +3 to -3. The bottom row shows the spatial polarization distribution, indicating the generation of vector beams with polarization order varies from +3 to -3. Consequently, it is feasible to generate different OAM-carrying vector beam with different OAM and polarization order through controlling the rotation rate of the slot antenna. In addition, the broadband property of the proposed metasurfaces has also been explored. The extinction ratio, defined as the ratio between the intensity of perpendicular and parallel components of the output beam with respect to the aperture direction, is used to characterize the quality of the generated OAM-carrying vector beam for different wavelength. Simulation results show that extinction ratio larger than 20 dB could be achieved over a bandwidth of 1500 nm (1000 nm–2500 nm). This device can be used to generate two types of OAM-carrying vector beam with opposite OAM charge sign by simply changing the handedness of the input beam, and its capability of working in broadband makes it attractive for many practical applications.

The present limit of the transmission type of nano-metallic surfaces is the low efficiency in light manipulation and phase shaping (up to approximately 10%), which is related to the optical loss in metals and small amount of the transmitted light. Reflection type metasurface is proposed to solve these two issues by adding a metallic ground plane on the back of the substrate that consists of
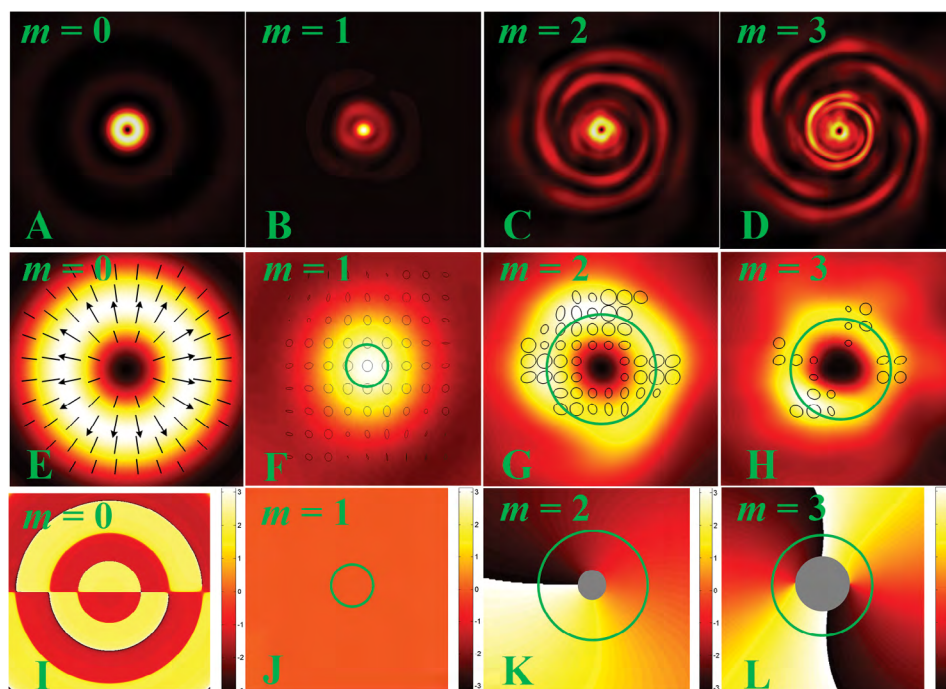
Figure 12 Numerical simulation results for 4-turn spiral structure with different geometric topological charge m. Top panel: intensity distribution, middle panel: polarization map superimposed on zoom-in intensity distribution, bottom panel: phase distribution of E_x for the main lobe. Adapted from Ref. [35].

a metal-insulator-metal configuration. The reflection type metasurfaces have been demonstrated to work in near IR with b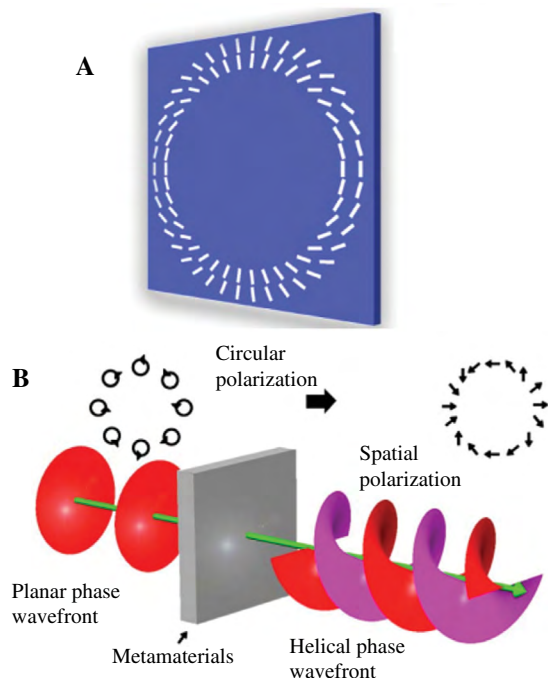roadband functionality and high efficiency (80% in theory) [46]. Recently, an alternative approach to reflection plasmonic metasurfaces has also been presented by replacing metallic plasmonic antennas with their dielectric counterparts, leading to increased efficiency (more than 98%) due to the reduced Ohmic loss [47]. Besides, the dielectric metasurface could also be operated at the transmission mode, a desirable feature for the realization of ultrathin optical elements [48], which have been successfully demonstrated to generate CV beam [49] and CV vortex beam [50]. The dielectric metasurface addresses an increasing need for low-cost and compact optical element without the ohmic loss.

Figure 13 (A) Schematic structure of metasurface for generating OAM-carrying vector beams. (B) Illustration of generation OAM-carrying vector beam. Adapted from Ref. [37].

5 Receiving optical complex fields with nano-metallic structures in the near field

The previous section concentrates on the nano-metallic surfaces based on optical scatters that scatter the SPPs excited by the free-space light or nanoscale emitters to the desired optical complex field in the far field. On the other hand, nano-metallic surfaces are also capable of receiving the optical complex field with high efficiency and distinguishing the optical complex field in terms of
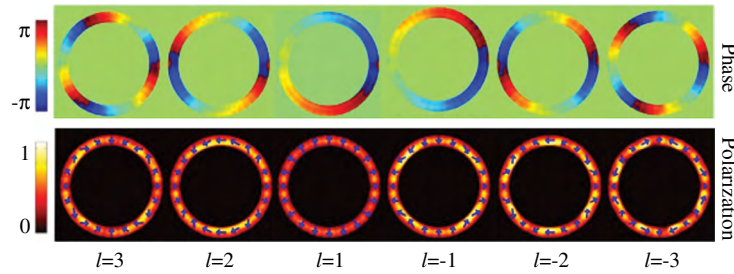
Figure 14 Spatial distributions of phase and polarization of generated OAM-carrying vector beams. Adapted from Ref. [37].

polarization, SAM and OAM in efficient and convenient way. In this case, instead of scattering the incident light into far field, the nano-metallic surfaces would convert the optical complex field into localized SPPs in the near field for further detection and analysis.

5.1 Plasmonic focusing of radially polarized beam with bull's eye plasmonic antenna

Within the context of antenna theory, the receiving antenna should match to the polarization mode pattern from the emitting antenna to maximize the received signal [40]. This is also true for plasmonic antennas for the purpose of localizing the incoming free space optical radiation into optimized plasmonic focal spots. In order to optimize the received signal, the illumination polarization pattern needs to match the corresponding polarization mode pattern that would radiate from the same plasmonic structure as if it were used as a transmitter. For example, the polarization of the emission from the bull's eye antenna is radially polarized, which means the receiving efficiency of the bull's eye antenna will be maximized with respect to the radially polarized illumination. This

optimal match could also be explained by the excitation requirement of the SPPs. When a radially polarized beam illuminates the circular slot, the entire beam is TM polarized with respect to the annular edge of the slit, providing an efficient way to generate highly focused SPPs through constructive interference and creating an enhanced local field compared with linear polarized illumination. Experiment has been conducted to confirm the focusing properties of bull's eye plasmonic antenna under radial polarization excitation [36]. The bull's eye structure is made of multiple concentric circular slot etched into a silver film by focused ion beam milling (FIB) and the SEM images of the samples are shown in Figure 15. The function of the multiple concentric circular slots is to enlarge the collecting area of incident photons so as to boost the SPPs generation efficiency. To obtain an enhanced local field at the center of the bull's eye structure, the period of the concentric rings need to match the SPPs wavelength such that the SPP excited at different slits are in phase and constructively interfere with each other at the geometrical center, producing stronger field enhancement than the single ring plasmonic antenna.

The SPPs intensity distribution near the silver/air interface was directly mapped by a collection mode near-field
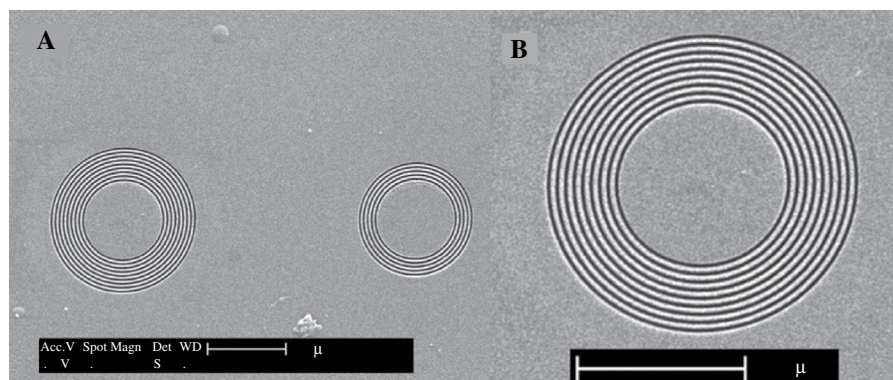

Figure 15 (A) SEM image of the bull's eye plasmonic antenna with 5-ring and 9-ring. (B) Zoom-in of the 9-ring plasmonic antenna. Adapted from Ref. [28].
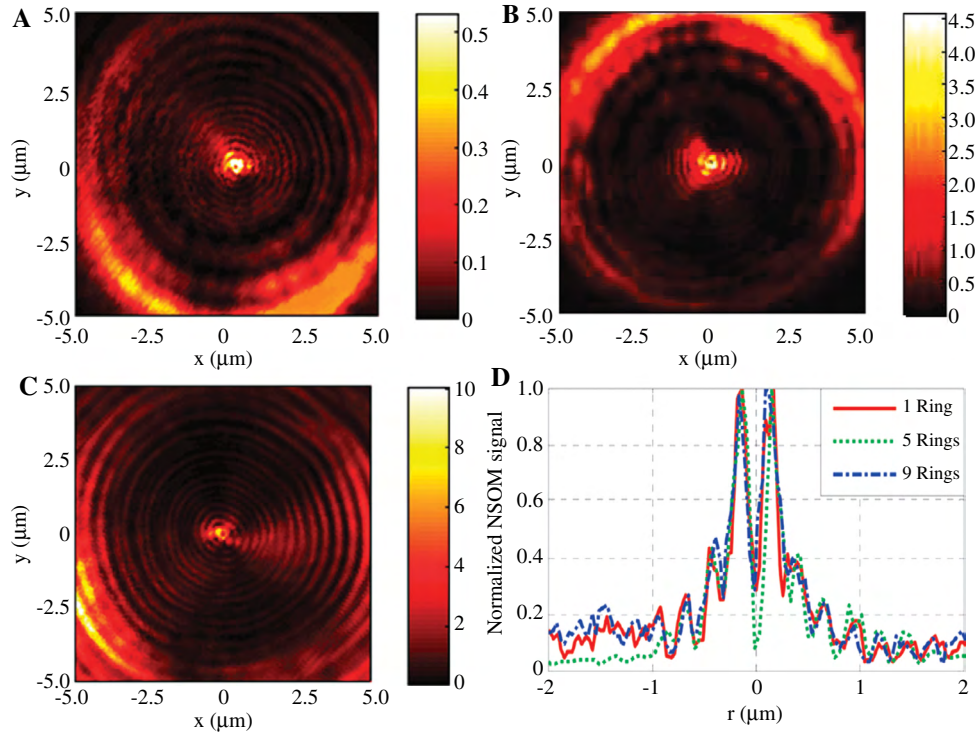
Figure 16 Measured near-field energy density distribution at the silver/air interface for (A) single ring (B) 5-ring and (C) 9-ring plasmonic antenna. (D) Measured normalized transverse profiles of energy density distribution through the center of bull's eye plasmonic antenna with single ring, 5-ring and 9-ring. Adapted from Ref. [28].

scanning optical microscope (NSOM). Figure 16A–C show the measured near-field energy density distribution for bull's eye plasmonic lens with different number of ring. Since a NSOM probe with tiny aperture was used in the experiment, the NSOM detected signal is proportional to $|\nabla_{\perp}E_z|^2$ [51], leading to a donut shape distribution with a very small dark center. By comparing the focusing intensity it can be seen that the focal field can be strengthened by adding more concentric rings satisfying the Bragg condition for the SPPs wavelength. However, note that the intensity of the focal field cannot keep increasing by adding more rings due to the propagation loss of the SPPs. A comparison of the transverse profiles of the measured plasmonic focal field for single ring, 5-ring and 7-ring is shown in Figure 16D. The main lobes of the three curves almost overlap with each other, indicating that the focal spot remains the same size as more rings are added to the bull's eye structure.

5.2 Spin dependence of spiral plasmonic antenna and metasurface

In RF antenna design, it is well known that the radiated mode is circularly polarized for an Archimedes' spiral slot antenna fabricated in a perfect conducting surface [40].

The handedness of the circular polarization depends on the handedness of the spiral. Thus, a spiral plasmonic antenna as a receiver will exhibit spin dependence on the illumination. Considering a left hand single turn spiral (LHS) etched into a thin metal film deposited on a glass substrate, the spiral with coordinates for calculation is shown in Figure 17A. A plane wave with circular polarization illuminates the structure normally from the glass substrate side. If the pitch of the spiral is chosen to be equal to the SPPs wavelength, simple analytical expressions can be derived to predict that the plasmonic field near the vicinity of the center of the plasmonic antenna. For RHC illumination, the plasmonic field in the vicinity of the center of the spiral can be given by [52]:

$$\vec{E}_{\text{SPP,RHC}}(\text{R},\theta)=\vec{e}_z\,2\pi E_{0z}r_0e^{-k_z z}e^{ik_r r_0}J_0(k_r\text{R}), \tag{7}$$

and the plasmonic field under LHC illumination will be [52]:

$$\vec{E}_{\text{SPP,LHC}}(\text{R},\theta)=\vec{e}_z\,2\pi E_{0z}r_0e^{-k_z z}e^{ik_r r_0}e^{2i\theta}J_2(k_r\text{R}). \tag{8}$$

Clearly the field distributions for RHC and LHC are spatially separated near the origin. For the LHS antenna, RHC illumination produces a solid spot in the center while LHC illumination creates a donut shape distribution. Similarly,
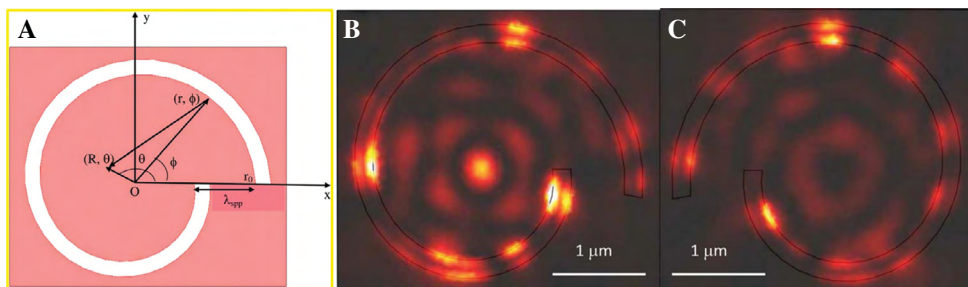
Figure 17 (A) Diagram of a LHS and the coordinates used in the calculation. Simulation results of the intensity distributions on (B) LHS and (C) RHS under RHC polarization illumination. Adapted from Ref. [41].

for a RHS antenna, RHC will produce a donut and LHC will create a solid spot. The analytical predications are validated by numerical simulations using finite element method. Figure 17B, C show the different plasmonic field distributions for LHS and RHS illuminated by RHC. The spin-dependent focusing of spiral plasmonic antenna has been experimentally confirmed by both near-field scanning optical microscopy [53] and two-photon fluorescence microscopy [54]. If a detector with a small enough diameter is placed at the origin, the detected signal should differentiate RHC and LHC polarizations, enabling a circular polarization analyzer design. Extinction ratio on the order of 100 has been predicted by the analytical model and experimentally confirmed. Such an extinction ratio level achieved by this fairly simple spiral antenna makes it attractive for applications in full Stokes' parameter polarimetric imaging.

The coupling efficiency of the plasmonic spiral antenna can be improved by a two-layer spiral design [55]. As shown in Figure 18A, in this design, the bottom layer has a wider spiral slot to capture the incident photonic energy as much as possible, while a second layer of spiral with narrower slot efficiently couples the plasmonic wave towards the center and maintains high extinction ratio. Instead of a subwavelength detector, a needle like plasmonic waveguide can be designed to effectively couple and channel the plasmonic wave adiabatically towards the needle apex through careful impedance matching design of a dielectric spacer. This kind of integrated structure can efficiently localize the incoming free space photonic energy into extremely subwavelength scale, a typical function of an antenna (simulation result is shown in Figure 18B). Compared to the bull's eye plasmonic lens and other type of rotationally symmetric plasmonic antenna structures with radially polarized excitation, the use of spiral antenna eliminates the needs of center alignment and makes parallel operation possible. The application of such structure in parallel optical near-field lithography and imaging has been proposed (Figure 18C, D).

The polarization states of the optical signal that can be coupled to a plasmonic lens are often limited by the selectivity of the coupling process. Only the component of the light that is polarized perpendicularly to the scattering elements can be coupled into SPPs, leading to a decrease in the SPPs signal and a loss of information about the incident polarization state. In the spiral slot antenna designs described above, the theoretical maximum efficiency is limited to about 50%. This can be understood through a linear decomposition of circular polarization state into radially and azimuthally polarized components. For the spiral slot antenna designs, only the radially polarized component can be coupled into SPPs, hence limiting the maximally attainable efficiency. In order to overcome this limit and improve the coupling efficiency, a hybrid spiral
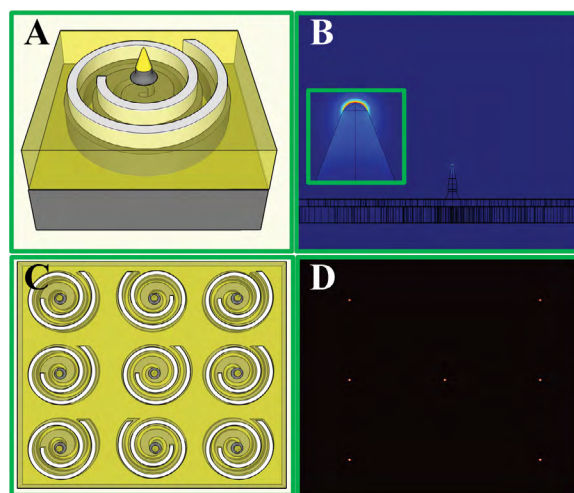

Figure 18 (A) Diagram of the proposed near-field plasmonic probe consisted of two spiral plasmonic antennas and a composite conical tip at the center. (B) Simulated intensity distribution on the probe with LHS plasmonic antenna under RHC polarized illumination. (C) Schematic drawing of an array of the near-field probe. The array consists of spirals with alternative handedness. (D) Simulated intensity distribution at 10 nm above the tip apex for RHC polarized illumination. Adapted from Ref. [44].

plasmonic antenna has been investigated. Utilizing the geometric phase effect, it has been demonstrated that isosceles triangular subwavelength apertures spatially arranged into a circle can be used to produce plasmonic focal field under azimuthally polarized illumination. Combining a spiral slot with spiral triangular subwavelength aperture antennas, a hybrid spiral antenna has been shown to improve the coupling efficiency to 94% [56, 57].

Besides focusing light with different SAM into spatial separated spots, it is useful to be able to route photons into specific directions according to the spin. A directional plasmonic coupler based on metasurface was proposed which enables polarization-controlled tunable directional coupling with polarization-invariant total conversion efficiency [58]. Figure 19A shows the SEM image of the metasurface comprised of multiple columns of apertures positioned in parallel. A narrow aperture in a metal film selectively scatter incident light that is polarized perpendicular to it, therefore the SPPs emission pattern of such a subwavelength aperture is approximately that of an in-plane dipole. If many such dipoles are arranges into a column with a spacing that is smaller than the SPPs wavelength, the launched SPPs are plane waves that propagate perpendicularly away toward either side of the column.

By putting multiple columns of the aperture array on the metal surface, the SPPs waves created by individual columns would interfere with each other, resulting in a complex polarization response. By changing the polarization state of the incident photons, the fraction of the total converted power that is propagating in the SPPs waves launched either toward the left or right side of the column pair can be adjusted. It has been confirmed in experiment that unidirectional coupling occurs when the incident light is circularly polarized, with the coupling direction determined by the spin of the photons. Figure 19B–D show the NSOM mapped near-field intensity distribution of the device back-illuminated by different polarizations. For incident photons with circular polarization, the propagating direction of the SPPs waves are opposite for different handedness of the circular polarization. In contrast, the launched SPPs have equal intensity toward either side of the coupler when the incident light is linearly polarized. Consequently, this structure is analogous to a polarizing beam splitter with two SPPs output channels. The polarization state of the incident light is then fully encoded in the amplitude and relative phase of the SPPs. In addition, this plasmonic coupler can be bent into a circle to achieve spin-dependent focus. Depending on the handedness of the structure, the SPPs waves launched by two
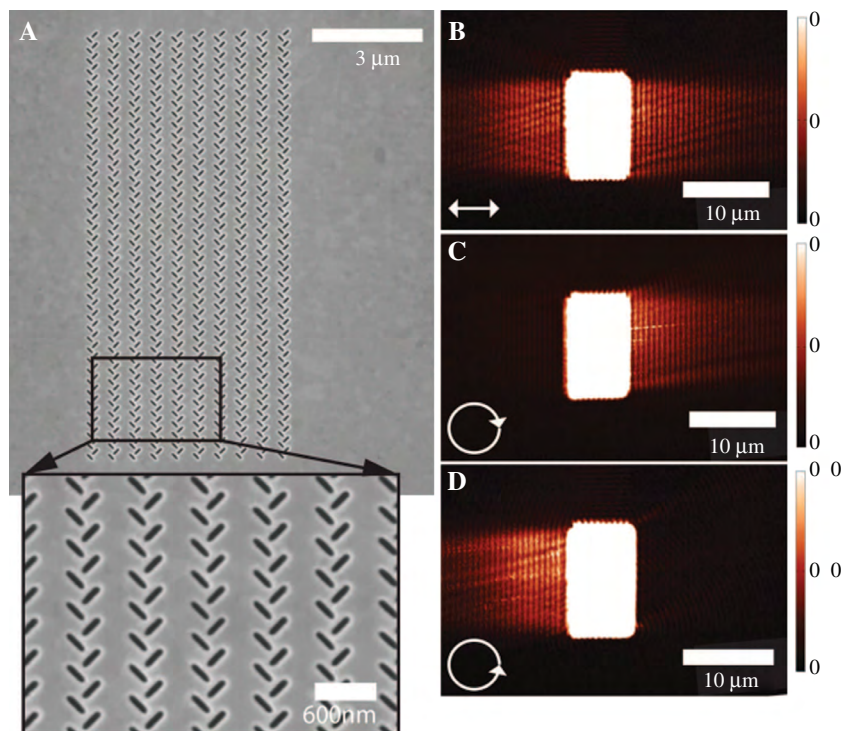

Figure 19 (A) SEM image of an array consists of multiple parallel column pairs of subwavelength apertures. NSOM images of the structure under illumination from the back by (B) linearly (C) RHC and (D) LHC polarized light. The state of incident polarization is indicated by white arrows. Adapted from Ref. [47].
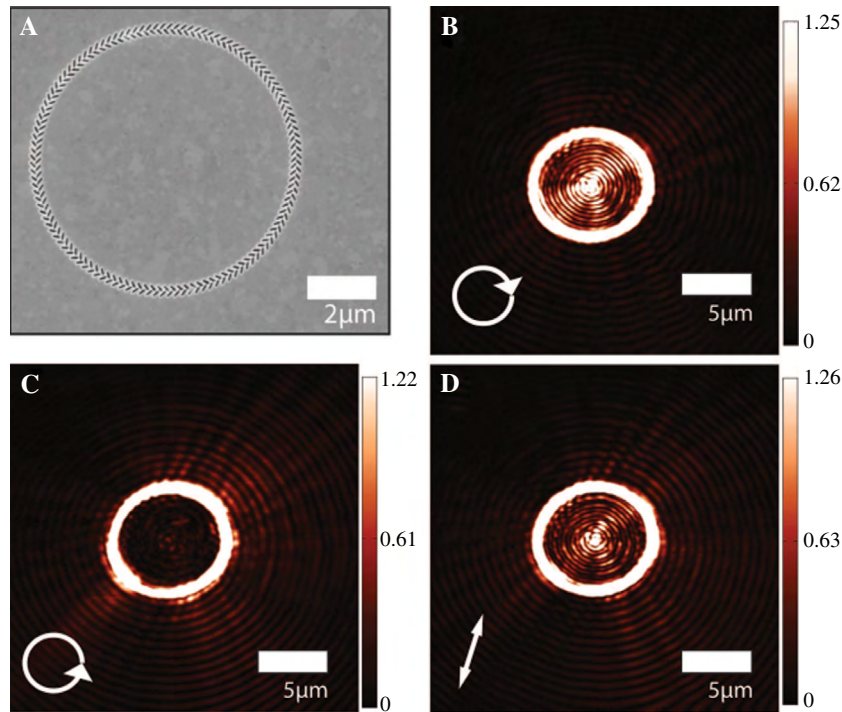
Figure 20 (A) SEM image of a circular coupler. NSOM images of the coupler under (B) RHC, (C) LHC and (D) linearly polarized light. The state of incident polarization is indicated by white arrows. Adapted from Ref. [47].

circular polarization states propagate radially towards to or outwards from the center of the center, respectively (Figure 20).

5.3 Detection of OAM states of light

In a wide range of applications that involve OAM, it is often crucial to discern different OAM states with high fidelity. Usually the topological charge carried by the beam is detected by the interference pattern between the vortex and a linearly polarized Gaussian beam, which requires tedious calibration and alignment work. Recently, a novel method for OAM detection using plasmonic photodiode was reported [59]. As shown in Figure 21A, the device can be regarded as metallic hologram with subwavelength resolution that carry information of the desired wavefront. Light coming at normal incidence is focused onto the holographic interface and coupled to a particular SPPs mode eventually propagating at the surface. The holographic fork-like coupler is designed to obtain topological charge L_g=1. Considering the AM conservation law, only the
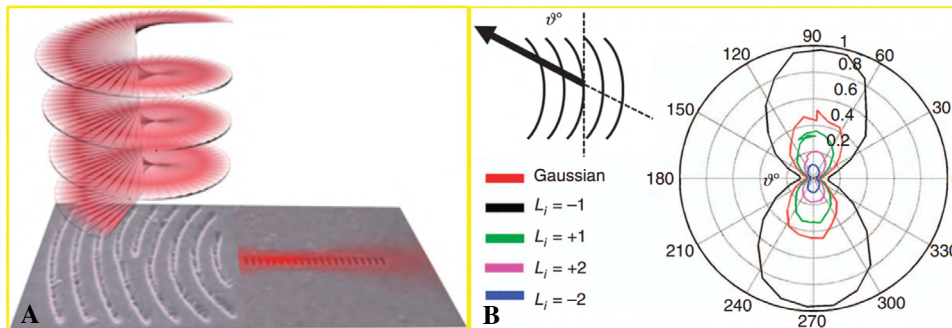

Figure 21 (A) A holographic coupler consists of curved and fork-shaped grooves that converts an incident vortex beam with topological charge of -1 into a focused surface wave propagating along the axis of the device, which is funneled through an array of subwavelength holes and then measured by a photodiode underneath the metal film. (B) Detected photocurrent as a function of the incident polarization for incident beams with different OAMs. The inset shows the orientation of the polarization of the incident electric field (represented by the arrow) with respect to the grooves. Adapted from Ref. [48].
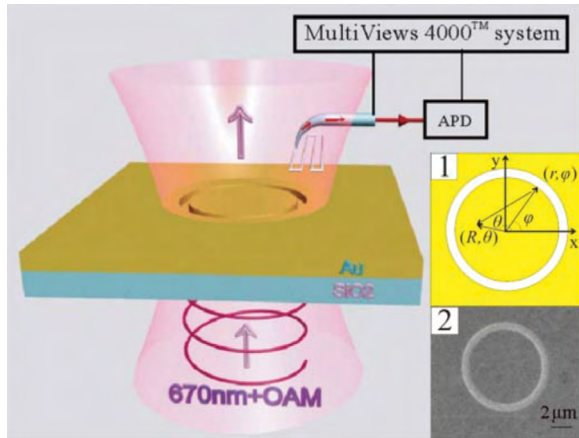
Figure 22 Schematic of the experimental setup. The plasmonic antenna is excited by LG mode from the substrate side and imaged by a NSOM probe. Inset 1 shows the diagram of a single ring plasmonic antenna. Inset 2 is the SEM image of the ring slot plasmonic antenna fabricated in gold film. Adapted from Ref. [49].

normally incident light with topological charge L_i=-1 can be focused. The focused light would be funneled through the metallic film by the array of subwavelength holes fabricated along the axis of the device, towards the surface of the photodiode underneath the device. For beam with any other topological charge, it will be defocused away from the array of holes therefore will not be detected by the diode. Figure 21B summarizes the experiment results for incident vortex beam with different topological charges. The maximum photocurrent is observed for an incident vortex beam with L_i=-1. Besides, it can be seen that the maximum signal is obtained for an incident polarization oriented normal to the grooves of the holographic interface.

The metallic hologram design presented above enables the realization of a compact and integrated OAM detection scheme, but only works for one specific OAM state. Recently a novel scheme enables multiple OAM states detecting was reported with circular slot plasmonic antenna [60]. Figure 22 shows the SEM image of the fabricated sample and experimental configuration. Linearly polarized Laguerre-Gaussian light carrying different OAM states normally illuminate the circular slot antenna from the substrate side. The near-field signals are captured by a NSOM probe working in collection mode. The transmitted optical field on the other side of the antenna is comprised of two parts: SPPs propagating along the metal/air surface and incident light that directly transmitted through the slot. The field patterns formed by SPPs wave and the directly transmitted wave interfere with each other and create a unique intensity profile that is highly dependent on the OAM state of the incident field. The OAM-dependent focusing property of the circular slot plasmonic antenna was confirmed experimentally. Figure 23 shows the collected near-field intensity distribution 200 nm above the sample surface excited by photons with different OAM states. Note that the transversal electric field is mainly collected due to the aperture of the probe used (~100 nm). When the illumination is fundamental Gaussian mode (l=0), the transverse components of the SPPs wave from the opposite sides of the circular slot interfere constructively at the center, leading to a solid spot. For $|l|$=1 and 2, donut-shaped spot and elliptical solid spot can be observed in the center, respectively. In addition, not only the intensity distribution allows the determination of the absolute value of the OAM, but also the rotation of the interference pattern (semi-arcs) gives the sign of the OAM. For example, the intensity distribution rotates anti-clockwise for l=1. Once the OAM changes to l=-1, the rotation direction become clockwise with the same angle. More interestingly, as the observation plane moves away from the surface of the sample, the fields arising from the
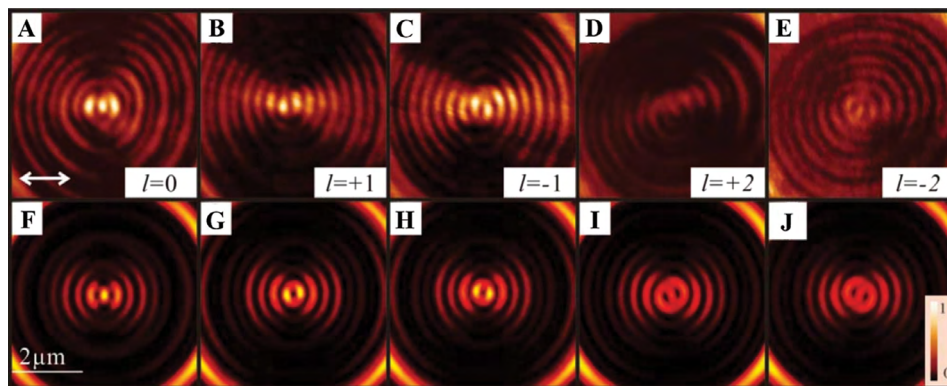

Figure 23 Intensity distribution of the optical field near the plasmonic antenna excited by light with different OAMs at the height of 200 nm over the antenna surface. (A)–(E) are the NSOM images for l=0, +1, -1, +2 and -2, respectively. (F)–(J) are the corresponding numerical simulation results. Adapted from Ref. [49].

SPPs decays exponentially in amplitude but maintains a constant phase pattern, while the directly transmitted field will accumulate phase shift due to the propagation. Such a difference in the phase behavior of the two contributing components causes a rotation of the interference pattern that also depends on the OAM state of the incident light. Figure 24 shows the simulated intensity distribution with different observation distance h for l=+1. When the distance between the sample plane and the observation plane increases, the rotation angle increases as shown in Figure 24H. By determining the intensity shape and rotation direction, this technology enable to determine both the absolute value and the sign of the incident OAM state with only one measurement of the intensity distribution at a plane above the sample surface but also within the near-field region.

6 Applications and perspectives

Benefiting from the flexibility in shaping the wavefront of light by introducing an abrupt interfacial phase discontinuity, metasurfaces have been used to achieve control over the propagation of light at an unprecedented level, a capability would open up myriad opportunities for applications. For example, one can envision the realization of metalens featured by broadband, aberration-free, and high NA, dramatically reducing the size, weight, and the complexity of current objectives that adopt multiple lenses to correct the aberration. Besides that, shaping the phase distribution of a light is very important for reconstructing

3D images, a technique that has been known as holography for several decades. Holographic techniques for controlling the amplitude and phase of light have been used to achieve beam shaping [61], data storage [62], SPP holographic displays [63], and optical trapping [64]. The usual way to generate the hologram is to calculate the phase information of the wave at the hologram interface and encoding the phase information into surface relief structures or spatial light modulators, which is referred to as computer-generated holography (CGH). Recently, 3D CGH image reconstruction in the visible range has been demonstrated by using ultrathin metasurface consisting of an array of subwavelength plasmonic antennas with defined orientations or varying sizes [65–67]. Using this technique, it is possible to efficiently control not only the phase but also the amplitude of the incident wave. In addition, metasurface-based hologram can potentially be expanded to realize active hologram working at nearly any frequency.

Since its introduction in 1992, optical field that carry OAM has kindled a huge activity in different lines of research, ranging from micro and nanoparticle trapping, optical lithography, astronomy, and optofluidics to optical telecommunication [68–72]. Additional to the aforementioned classical applications, optical OAM opens up a promising perspective in quantum information science. For example, OAM can be utilized for qudit systems that allow entanglement of OAM photons [73], quantum coin-tossing [74], and improved security for quantum key distribution [75], etc. As for the CV beams, the spatial separation between the longitudinal and transversal components of the focal field for highly focused CV beams leads
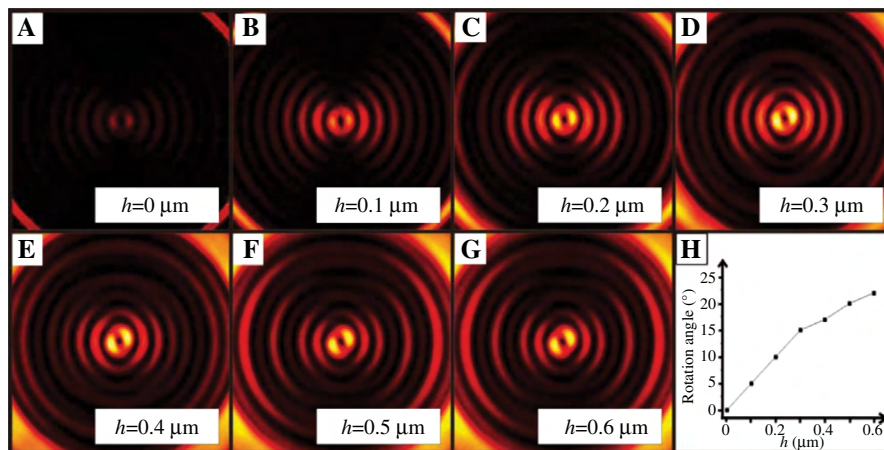

Figure 24 Intensity distribution of the optical field near the plasmonic antenna for l=+1 with different tip-sample distance h of (A) 0 μm, (B) 0.1 μm, (C) 0.2 μm, (D) 0.3 μm, (E) 0.4 μm, (F) 0.5 μm and (G) 0.6 μm. (H) The rotation angle versus the tip-sample distance h. Adapted from Ref. [49].

to a variety of applications in optical focus engineering. Through phase modulation at the pupil plane with diffractive optical elements with multiple concentric zones, optical focal fields with different desirable characteristics have been demonstrated with the use of CV beams, such as flattop [76], optical bubbles [77], optical chain [78] and optical needle [79]. The possibility of producing a unique focal field distribution with CV beams naturally finds many applications that require the use of tightly focused light beams, such as dielectric and metallic nanoparticle trapping [3, 80], laser micromachining [2], laser direct writing [81], optical imaging [82] and so on. Nevertheless, with the rapid development of nano-metallic surfaces, it is safe to conclude that simple and efficient generation and detection method for optical complex fields become more and more accessible, leading to further in-depth research and rapidly expanded applications in this field.

Compared with the conventional photonic devices to impose specific forms of spatially varying modulation on a beam of light, such as the bulk dielectric optical element and SLM, nano-metallic surfaces provide great flexibility and functionality as the optical wavefront can be tailored at will by forming a spatially varying optical response (in amplitude, phase as well as the polarization) with thin film made of lossy materials. Compared with volume metamaterials, the metasurfaces offer the advantage of being lighter, easier to fabricate and less lossy due to the reduced dimensionality. The disadvantage of using nano-metallic surfaces is that they typically suffer from low efficiency due to the weak coupling between the incident and cross-polarized optical fields. Possible solutions to increase efficiency include the use of materials with more complexity [83, 84], employing device working away from the resonance [85], and combining the metallic antennas with a reflective ground plane [46, 86]. However, ohmic losses in metal still pose a limit to the achievable efficiency at optical wavelengths. High-refractive-index resonant dielectric metasurface offers an alternative solution to the issue of material (non-radiative) loss. Such metasurfaces exhibit magnetic and electric dipole, and higher order Mie resonances while suffering from much less absorption loss than their metallic counterparts. Furthermore, dielectric metasurfaces offer other potential benefits such as high transmission and wide bandwidth. However, the materials available for constructing dielectric metasurface at optical wavelength are limited by the requirement of high refractive index. In addition, in contrary to nano-metallic surfaces, realization of amplitude modulation by dielectric metasurfaces remains challenging, which subsequently hampers their capabilities in tailoring optical fields at will.

Finally, the discussion of optical complex field in this review has been limited to the spatial domain. However, it is worthy of noting that the engineering of optical field in the temporal domain would add one more degree of freedom that can be used to match dispersion properties of the engineered materials. We envision that a spatiotemporally comprehensively tailored optical complex field and its interaction with correspondingly engineered nano-metallic surfaces and metamaterials will provide much more rich physical phenomena that deserves further studies.

7 Conclusions

This paper reviews the rapid growth in the field of interactions between optical complex field and nano-metallic surfaces. The combination of optical complex field and nano-metallic surfaces results in plenty of benefits, rendering the nano-metallic surfaces a promising platform to explore complex optical effects and new applications. Recent progress in plasmonic antennas and metasurfaces address the major issues hampering the full-scale development of nanophotonics and metamaterials, such as high loss, cost-ineffective fabrication and challenging integration. Nano-metallic surfaces have several attractive features that may provide viable solutions to these challenges. For example, the strong local field enhancement leads to stronger light-matter interaction, through which many weak processes can be enhanced and effectively utilized. The combination of the tight field confinement and ultrafast optical process offered by nonlinear optical materials may enable the construction of miniaturized devices for the development of high speed and high density photonic circuits. The last not the least, the characteristics of the nano-metallic surfaces are highly tunable through altering the incident optical complex field and adjusting the responses of individual optical antenna element and their coupling. The alliance of optical complex field and nano-metallic surfaces will undoubtfully lead to the development of new types of nano-metallic devices with novel functionalities and significantly improved performance.

References

[1] Sheppard CJR, Choudhury A. Annular pupils, radial polarization, and superresolution. Appl Opt 2004;43:4322–7.

[2] Meier M, Romano V, Feurer T. Material processing with pulsed radially and azimuthally polarized laser radiation. Appl Phys A 2007;86:329–34.

[3] Zhan Q. Trapping metallic Rayleigh particles with radial polarization. Opt Express 2004;12:3377–82.

[4] Zhan Q, Leger JR. Microellipsometer with radial symmetry. Appl Opt 2002;41:4630–7.

[5] Milione G, Sztul HI, Alfano RR. Stokes polarimetry of a hybrid vector beam from a spun elliptical core optical fiber. Complex Light and Optical Forces IV, Proc. of SPIE 2010;7613:761305.

[6] Moreno I, Davis JA, Hernandez TM, Cottrell DM, Sand D. Complete polarization control of light from a liquid crystal spatial light modulator. Opt Express 2012;20:364–76.

[7] Maluenda D, Juvells I, Martínez-Herrero R, Carnicer A. Reconfigurable beams with arbitrary polarization and shape distributions at a given plane. Opt Express 2013;21:5432–9.

[8] Han W, Yang Y, Cheng W, Zhan Q. Vectorial optical field generator for the creation of arbitrarily complex fields. Opt Express 2013;21:20692–706.

[9] Yu N, Genevet P, Kats MA, Aieta F, Tetienne J-P, Capasso F, Gaburro Z. Light propagation with phase discontinuities: generalized laws of reflection and refraction. Science 2011;334:333–7.

[10] Joannopoulos JD, Villeneuve PR, Fan S. Photonic crystals: putting a new twist on light. Nature 1997;386:143–9.

[11] Liu Y, Zhang X. Metamaterials: a new frontier of science and technology. Chem Soc Rev 2011;40:2494–507.

[12] Yu N, Capasso F. Flat optics with designer metasurfaces. Nat Mater 2014;13:139–50.

[13] Neu J, Krolla B, Paul O, Reinhard B, Beigang R, Rahm M. Metamaterial-based gradient index lens with strong focusing in the THz frequency range. Opt Express 2010;18:27748–57.

[14] Olson J, Manjavacas A, Liu L, Chang W-S, Foerster B, King NS, Knight MW, Nordlander P, Halas NJ, Link S. Vivid, full-color aluminum plasmonic pixels. Proc Natl Acad Sci 2014;111:14348–14353.

[15] Kim W-C, Park N-C, Yoon Y-J, Choi H, Park Y-P. Investigation of near-field imaging characteristics of radial polarization for application to optical data storage. Opt Rev 2007;14:236–42.

[16] Stevens CJ, Chan CWT, Stamatis K, Edwards DJ. Magnetic metamaterials as 1-D data transfer channels: an application for magneto-inductive waves. microwave theory and techniques. IEEE Trans 2010;58:1248–56.

[17] Bautista G, Huttunen MJ, Kontio JM, Simonen J, Kauranen M. Third- and second-harmonic generation microscopy of individual metal nanocones using cylindrical vector beams. Opt Express 2013;21:21918–23.

[18] Chen R, Agarwal K, Sheppard CJR, Chen X. Imaging using cylindrical vector beams in a high-numerical-aperture microscopy system. Opt Lett 2013;38:3111–4.

[19] Fraine A, Uribe-Patarroyo N, Simon DS, Minaeva O, Sergienko AV. Object identification using correlated orbital angular momentum states. Lasers and Electro-Optics (CLEO), 2013 Conference on; 2013 9–14 June 2013; 2013. pp. 1–2.

[20] Yan J, Lu Y, Wang P, Gu C, Zheng R, Chen Y, Ming H, Zhan Q. Improving the sensitivity of fiber-optic SPR sensor via radially polarized beam excitation. Chin Opt Lett 2009;7:909–11.

[21] Dennis MR, O'Holleran K, Padgett MJ. Chapter 5 Singular optics: optical vortices and polarization singularities. In: Progress in Optics, Volume 53. Elsevier, 2009. pp. 293–363.

[22] Soskin MS, Vasnetsov MV. Chapter 4 Singular optics. In: Wolf E, eds. Progress in optics, Volume 42. Amsterdam, Elsevier, 2001, pp. 219–76.

[23] Zhan Q. Cylindrical vector beams: from mathematical concepts to applications. Adv Opt Photon 2009;1:1–57.

[24] Barnes WL, Dereux A, Ebbesen TW. Surface plasmon subwavelength optics. Nature 2003;424:824–30.

[25] Bharadwaj P, Deutsch B, Novotny L. Optical antennas. Adv Opt Photon 2009;1:438–83.

[26] Ruan Z, Qiu M. Enhanced transmission through periodic arrays of subwavelength holes: the role of localized waveguide resonances. Phys Rev Lett 2006;96:233901.

[27] Marrucci L, Manzo C, Paparo D. Optical spin-to-orbital angular momentum conversion in inhomogeneous anisotropic media. Phys Rev Lett 2006;96:163905.

[28] Berry MV. The adiabatic phase and pancharatnam's phase for polarized light. J Mod Opt 1987;34:1401–7.

[29] Shitrit N, Bretner I, Gorodetski Y, Kleiner V, Hasman E. Optical spin hall effects in plasmonic chains. Nano Lett 2011;11:2038–42.

[30] Huang L, Chen X, Mühlenbernd H, Li G, Bai B, Tan Q, Jin G, Zentgraf T, Zhang S. Dispersionless phase discontinuities for controlling light propagation. Nano Lett 2012;12:5750–5.

[31] Chen X, Huang L, Mühlenbernd H, Li G, Bai B, Tan Q, Jin G, Qiu C-W, Zhang S, Zentgraf T. Dual-polarity plasmonic metalens for visible light. Nat Commun 2012;3:1198.

[32] Gorodetski Y, Shitrit N, Bretner I, Kleiner V, Hasman E. Observation of optical spin symmetry breaking in nanoapertures. Nano Lett 2009;9:3016–9.

[33] Yu N, Genevet P, Aieta F, Kats MA, Blanchard R, Aoust G, Tetienne JP, Gaburro Z, Capasso F. Flat optics: controlling wavefronts with optical antenna metasurfaces. IEEE J Sel Top Quantum Electron 2013;19:4700423–4700423.

[34] Aieta F, Genevet P, Kats MA, Yu N, Blanchard R, Gaburro Z, Capasso F. Aberration-free ultrathin flat lenses and axicons at telecom wavelengths based on plasmonic metasurfaces. Nano Lett 2012;12:4932–6.

[35] Ni X, Ishii S, Kildishev AV, Shalaev VM. Ultra-thin, planar, Babinet-inverted plasmonic metalenses. Light Sci Appl 2013;2:e72.

[36] Chen W, Abeysinghe DC, Nelson RL, Zhan Q. Plasmonic lens made of multiple concentric metallic rings under radially polarized illumination. Nano Lett 2009;9:4320–5.

[37] Rui G, Chen W, Lu Y, Wang P, Ming H, Zhan Q. Plasmonic near-field probe using the combination of concentric rings and conical tip under radial polarization illumination. J Opt 2010;12:035004.

[38] Chen W, Han W, Abeysinghe DC, Nelson RL, Zhan Q. Generating cylindrical vector beams with subwavelength concentric metallic gratings fabricated on optical fibers. J Opt 2011;13:015003.

[39] Lin J, Genevet P, Kats MA, Antoniou N, Capasso F. Nanostructured holograms for broadband manipulation of vector beams. Nano Lett 2013;13:4269–74.

[40] Kraus JD, Marhefka RJ. Antennas for all Applications, 3rd ed., New York, USA, McGraw-Hill, 2002.

[41] Rui G, Nelson RL, Zhan Q. Circularly polarized unidirectional emission via a coupled plasmonic spiral antenna. Opt Lett 2011;36:4533–5.

[42] Rui G, Chen W, Abeysinghe DC, Nelson RL, Zhan Q. Beaming circularly polarized photons from quantum dots coupled with plasmonic spiral antenna. Opt Express 2012;20:19297–304.

[43] Rui G, Nelson RL, Zhan Q. Beaming photons with spin and orbital angular momentum via a dipole-coupled plasmonic spiral antenna. Opt Express 2012;20:18819–26.

[44] Rui G, Abeysinghe DC, Nelson RL, Zhan Q. Demonstration of beam steering via dipole-coupled plasmonic spiral antenna. Sci Rep 2013;3:7.

[45] Zhao Z, Wang J, Li S, Willner AE. Metamaterials-based broadband generation of orbital angular momentum carrying vector beams. Opt Lett 2013;38:932–4.

[46] Sun S, Yang K-Y, Wang C-M, Juan T-K, Chen WT, Liao CY, He Q, Xiao S, Kung W-T, Guo G-Y, Zhou L, Tsai DP. High-efficiency broadband anomalous reflection by gradient meta-surfaces. Nano Lett 2012;12:6223–9.

[47] Yang Y, Wang W, Moitra P, Kravchenko II, Briggs DP, Valentine J. Dielectric meta-reflectarray for broadband linear polarization conversion and optical vortex generation. Nano Lett 2014;14:1394–9.

[48] Lin D, Fan P, Hasman E, Brongersma ML. Dielectric gradient metasurface optical elements. Science 2014;345:298–302.

[49] Liu Y, Ling X, Yi X, Zhou X, Luo H, Wen S. Realization of polarization evolution on higher-order Poincaré sphere with metasurface. Appl Phys Lett 2014;104:191110.

[50] Yi X, Ling X, Zhang Z, Li Y, Zhou X, Liu Y, Chen S, Luo H, Wen S. Generation of cylindrical vector vortex beams by two cascaded metasurfaces. Opt Express 2014;22:17207–15.

[51] Bouhelier A, Ignatovich F, Bruyant A, Huang C, Colas des Francs G, Weeber JC, Dereux A, Wiederrecht GP, Novotny L. Surface plasmon interference excited by tightly focused laser beams. Opt Lett 2007;32:2535–7.

[52] Yang S, Chen W, Nelson RL, Zhan Q. Miniature circular polarization analyzer with spiral plasmonic lens. Opt Lett 2009;34:3047–9.

[53] Chen W, Abeysinghe DC, Nelson RL, Zhan Q. Experimental confirmation of miniature spiral plasmonic lens as a circular polarization analyzer. Nano Lett 2010;10:2075–9.

[54] Wu Z, Chen W, Abeysinghe DC, Nelson RL, Zhan Q. Two-photon fluorescence characterization of spiral plasmonic lenses as circular polarization analyzers. Opt Lett 2010;35:1755–7.

[55] Rui G, Chen W, Zhan Q. High efficiency plasmonic probe design for parallel near-field optics applications. Opt Express 2011;19:5187–95.

[56] Chen W, Nelson RL, Zhan Q. Efficient miniature circular polarization analyzer design using hybrid spiral plasmonic lens. Opt Lett 2012;37:1442–4.

[57] Chen W, Rui G, Abeysinghe DC, Nelson RL, Zhan Q. Hybrid spiral plasmonic lens: towards an efficient miniature circular polarization analyzer. Opt Express 2012;20:26299–307.

[58] Lin J, Mueller JPB, Wang Q, Yuan G, Antoniou N, Yuan X-C, Capasso F. Polarization-controlled tunable directional coupling of surface plasmon polaritons. Science 2013;340:331–4.

[59] Genevet P, Lin J, Kats MA, Capasso F. Holographic detection of the orbital angular momentum of light with plasmonic photodiodes. Nat Commun 2012;3:1278.

[60] Liu A, Xiong X, Ren X, Cai Y, Rui G, Zhan Q, Guo G, Guo G. Detecting orbital angular momentum through division-of-amplitude interference with a circular plasmonic lens. Sci Rep 2013;3:5.

[61] Dolev I, Epstein I, Arie A. Surface-plasmon holographic beam shaping. Phys Rev Lett 2012;109:203903.

[62] Pégard NC, Fleischer JW. Optimizing holographic data storage using a fractional Fourier transform. Opt Lett 2011;36:2551–3.

[63] Ozaki M, Kato J-I, Kawata S. Surface-plasmon holography with white-light illumination. Science 2011;332:218–20.

[64] Grier DG. A revolution in optical manipulation. Nature 2003;424:810–6.

[65] Huang L, Chen X, Mühlenbernd H, Zhang H, Chen S, Bai B, Tan Q, Jin G, Cheah K-W, Qiu C-W, Li J, Zentgraf T, Zhang S. Three-dimensional optical holography using a plasmonic metasurface. Nat Commun 2013;4:2808.

[66] Ni X, Kildishev AV, Shalaev VM. Metasurface holograms for visible light. Nat Commun 2013;4:2807.

[67] Chen WT, Yang KY, Wang CM, Huang YW, Sun G, Chiang ID, Liao CY, Hsu WL, Lin HT, Sun S, Zhou L, Liu AQ, Tsai DP. High-efficiency broadband meta-hologram with polarization-controlled dual images. Nano Lett 2014;14:225–230.

[68] Gibson G, Courtial J, Padgett M, Vasnetsov M, Pas'ko V, Barnett S, Franke-Arnold S. Free-space information transfer using light beams carrying orbital angular momentum. Opt Express 2004;12:5448–56.

[69] Bhattacharya M, Meystre P. Using a Laguerre-Gaussian beam to trap and cool the rotational motion of a mirror. Phys Rev Lett 2007;99:153603.

[70] Wang H, Shi L, Lukyanchuk B, Sheppard C, Chong CT. Creation of a needle of longitudinally polarized light in vacuum using binary optics. Nat Photon 2008;2:501–5.

[71] Hell SW. Far-field optical nanoscopy. Science 2007;316:1153–8.

[72] Paterson L, MacDonald MP, Arlt J, Sibbett W, Bryant PE, Dholakia K. controlled rotation of optically trapped microscopic particles. Science 2001;292:912–4.

[73] Pors B-J, Monken CH, Eliel ER, Woerdman JP. Transport of orbital-angular-momentum entanglement through a turbulent atmosphere. Opt Express 2011;19:6671–83.

[74] Molina-Terriza G, Vaziri A, Ursin R, Zeilinger A. Experimental quantum coin tossing. Phys Rev Lett 2005;94:040501.

[75] Cerf NJ, Bourennane M, Karlsson A, Gisin N. Security of quantum key distribution using d-level systems. Phys Rev Lett 2002;88:127902.

[76] Zhan Q, Leger J. Focus shaping using cylindrical vector beams. Opt Express 2002;10:324–31.

[77] Chen W, Zhan Q. Three-dimensional focus shaping with cylindrical vector beams. Opt Commun 2006;265:411–7.

[78] Zhao Y, Zhan Q, Zhang Y, Li Y-P. Creation of a three-dimensional optical chain for controllable particle delivery. Opt Lett 2005;30:848–50.

[79] Wang J, Chen W, Zhan Q. Engineering of high purity ultra-long optical needle field through reversing the electric dipole array radiation. Opt Express 2010;18:21965–72.

[80] Zhan Q. Radiation forces on a dielectric sphere produced by highly focused cylindrical vector beams. J Opt A 2003;5:229–32.

[81] Beresna M, Gecevičius M, Kazansky PG, Gertus T. Radially polarized optical vortex converter created by femtosecond laser nanostructuring of glass. Appl Phys Lett 2011;98:201101.

[82] Chen W, Zhan Q. Creating a spherical focal spot with spatially modulated radial polarization in 4Pi microscopy. Opt Lett 2009;34:2444–6.

[83] Pfeiffer C, Grbic A. Metamaterial huygens' surfaces: tailoring wave fronts with reflectionless sheets. Phys Rev Lett 2013;110:197401.

[84] Monticone F, Estakhri NM, Alù A. Full control of nanoscale optical transmission with a composite metascreen. Phys Rev Lett 2013;110:203903.

[85] Zhao Y, Alù A. Tailoring the dispersion of plasmonic nanorods to realize broadband optical meta-waveplates. Nano Lett 2013;13:1086–91.

[86] Pors A, Nielsen MG, Eriksen RL, Bozhevolnyi SI. Broadband focusing flat mirrors based on plasmonic gradient metasurfaces. Nano Lett 2013;13:829–34.